Review of Aeronautical Fatigue Investigations in Germany During the Period May 2005 to April 2007

Dr. Claudio Dalle Donne
Pascal Vermeer
EADS Innovation Works Germany
CTO/IW/MS

CTO/IW/MS-2007-042 Technical Report
EADS Innovation Works

Title

Review of Aeronautical Fatigue Investigations in Germany During the Period May 2005 to April 2007

Authors
Dr. Claudio Dalle Donne
Pascal Vermeer

Project-No.

Phone	Department/Work area	Date	Report-Nr.
+49-89.607 27728	CTO/IW/MS	14/05/2007	CTO/IW/MS-2007-042

Abstract

Within the scope of the 2007 Meeting of the International Committee on Aeronautical Fatigue in Naples, this review embodies a compilation of abstracts on aeronautical fatigue investigations in Germany during the period May 2005 to April 2007.

The contribution of summaries by German aerospace manufacturers, governmental and private research institutes, universities as well as aerospace authorities was completely voluntary, and is acknowledged with sincere appreciation by the authors of this review.

Enquiries concerning the contents should be addressed directly to the author of the corresponding summary.

Distribution to
SC/IRT/IW-SP-Patents (e-mail to Fr. Rotter)
M&W Zander/FM-K2-OT-MF – microfilm
Coverpage: CTO/IW/L – Yann Barbaux, CTO/IW/IW – Stefan Lindemann (per e-mail in pdf.format)

pages	figures	drawings	diagrams	tables
54	52			

Keywords for database
Aeronautical fatigue, ICAF2007

[1] Classification
1 generally accessible
2 free distribution inside EADS
3 confidential
4 highly confidential

Acceptance

Dr. Dalle Donne
Head of responsible department

Table of contents

1 Introduction

Within the scope of the 2007 Meeting of the International Committee on Aeronautical Fatigue in Naples, this review embodies a compilation of abstracts on aeronautical fatigue investigations in Germany during the period May 2005 to April 2007.

The contribution of summaries by German aerospace manufacturers, governmental and private research institutes, universities as well as aerospace authorities was completely voluntary, and is acknowledged with sincere appreciation by the authors of this review.

Enquiries concerning the contents should be addressed directly to the author of the corresponding summary.

Mailing addresses of contributing companies and institutes:

Airbus-D	Airbus Deutschland GmbH, Kreetslag 10, 21129 Hamburg, www.airbus.com
EADS-IW	European Aeronautic Defence and Space Company, Innovation Works, 81663 Munich, www.eads.net
EADS-MAS	European Aeronautic Defence and Space Company, Military Air Systems, 81663 Munich, www.eads.net
DLR	German Aerospace Center DLR, Institute of Materials Research, 51170 Cologne, www.dlr.de
High-End	HIGH-END Engineering GmbH, Georg-Heyken-Straße 4, 21147 Hamburg, www.hee.de
IABG	Industrieanlagen-Betriebsgesellschaft mbH, PO-Box 1212, 85503 Ottobrunn, www.iabg.de
IMA	Materialforschung und Anwendungstechnik GmbH, PO-Box 800144, 01101 Dresden, www.ima-dresden.de
UniBw-M	University of the Federal Armed Forces Munich, Department of Materials Science, 85577 Neubiberg, www.unibw.de
Uni-Parma	Università degli studi di Parma, Via Università 12, 43100 Parma, Italy, www.unipr.it
Uni-Siegen	Institut für Werkstofftechnik, Universität Siegen, 57068 Siegen, www.uni-siegen.de
Rolls-Royce	Rolls-Royce Deutschland Ltd & Co KG, Eschenweg 11, Dahlewitz, 15827 Blankenfelde-Mahlow, www.rolls-royce.com/deutschland
RUAG	RUAG Aerospace Services GmbH, Airport Oberpfaffenhofen, PO-Box 1253, 82231 Wessling, www.ruag-aerospace-deutschland.com
TU-Dresden	Dresden University of Technology (TU), Institute of Materials Science, D-01062 Dresden, www.tu-dresden.de
WIWEB	Bundesamtes für Wehrtechnik und Beschaffung, Wehrwissenschaftliches Institut für Werk-, Explosiv- und Betriebsstoffe (WIWEB), Institutsweg 1, 85435 Erding, www.bwb.org
ZF-L	ZF Luftfahrttechnik GmbH, Flugplatzstraße, 34379 Calden, www.zf.com

2 Full Scale Testing

A380 Full-Scale Fatigue Test – News Flash 2006

After having accomplished the A380 structural fatigue certification milestone in December 2005 already, IABG further proceeded the A380 full-scale fatigue test on its Dresden site throughout the year 2006.

On November 05th, 2006 the next milestone has been successfully reached: After accomplishment of its 19.000th simulated flight the A380 has proven its fatigue-worthiness for one complete design life in accordance with the guaranteed design life goals. The test will go on for another 1,5 design lives.

A400M Full-Scale Fatigue Test – News Flash 2006

In the second quarter of 2006 the Dresden branch of IABG started the conceptual design work for the test set-up of the A400M full-scale fatigue test.

All preparatory work for the erection of a new IABG test hangar in Dresden – dedicated for the A400M full-scale fatigue test – has been accomplished in time.

The erection of the test hangar itself and the selection of suppliers will be the next steps in 2007.

2.1 Overview of Full Scale Fatigue Tests (May 2007)

Project	Customer	Test Structure	Schedule	Test Lab
A380	Airbus-D	Rear end test: Damage tolerance certification test of CFRP parts	2005-2006	Airbus-D
A380	Airbus-D	Full scale certification test of the complete inner flap	2005-2007	Airbus-D
A380	Airbus-F	Engine pylon fwd. attachment	2004-2006	IABG
A380	Patria	Spoiler no. 1 and no. 4	2004-2006	IABG
A380	Airbus-D	A380 Full scale fatigue test	2003-2008	IABG-IMA
PC21	Pilatus	Complete airframe	2004-2006	IABG
A380	Airbus-D	A380 Vertical Tail Plane fatigue and margin research test	2006-2007	IABG
A400M	Airbus-D	A400M Full scale fatigue test	2006-2010	IABG
Tay Engine	RRD	Tay LP Shaft assembly fatigue test	2006-2008	IABG
TP400	RRD	TP400 IMC Static and fatigue test program	2006-2007	IMA
A380	Airbus-D	Flap track no. 6 static and fatigue certification test	2004-2007	IMA
A380	Airbus-D	Flap carriage no. 3 crack propagation development test	2005-2007	IMA
IARCAS	Airbus-D	Fatigue of fuselage panels with repair solutions IARCAS	2005-2006	IMA
A380	Eurocopter-D	Passenger door torsion bar test - strength and fatigue test	2005-2006	IMA
M-346	Liebherr	Nose landing gear test - NLG stiffness, strength and fatigue test	2005-2006	IMA
EFA	NETMA	Wing attachment box	2001-2006	EADS-MAS
A380	Airbus-F	Engine pylon shackle test	2005-2006	EADS-MAS
400M	MAS	C72 Frame static, fatigue and DT test	2006-2007	EADS-MAS
Research	Airbus-D	6 Bar linkage system test	2006-2007	EADS-MAS
Research	Airbus-D	4 Bar linkage system test	2007-2008	EADS-MAS

2.2 AIRBUS A380 Vertical Tail Plane Leading Edge Loading Capacity Test

Peters and G. Hilfer (IABG)

A section of the vertical tail plane leading edge of Airbus A380 was exposed to static and fatigue testing including damage tolerance investigations at the IABG test laboratories in Ottobrunn, Germany. The test specimen consisted of the ribs 9 up to 12, the LE spar assemblies, the D nose assembly with ribs and the LH and RH LE panels. The effective test area was the middle part of the test article. This part of the A380 vertical tail plane was tested to demonstrate the static strength of the panels. Furthermore, the fatigue and damage tolerance tests were to fulfil the certification requirements of the D nose.

The test specimen was supported at two points by a support structure equivalent to the stiffness of the adjacent a/c structure. The support structure was mounted on the Modular Test Area (MTA) of IABG via an adapter plate (Figure 1). The loading of the test specimen was introduced by 3 hydraulic actuators all acting in Y-direction at 3 points on the D nose.

Some impact damages were introduced into the test specimen before installation into the test rig. Further damages were introduced into the test specimen before the damage tolerance test phase was started. The test specimen was instrumented for the performance of the required static measurement tests with 105 sensor channels.

The test specimen was loaded in a first step by a static test to demonstrate the static strength and to compare the test results with the FEM calculation results. Furthermore, the test specimen was exposed to fatigue testing and to damage tolerance testing simulating the loading within 1.5 aircraft lives. Finally a margin research test was performed applying static load.

Figure 1 Test Set-up arrangement of the MTA

2.3 Fatigue Analysis and Life Extension of the Lower Planetary Carrier Plate of CH-53 Helicopter

W. Kreuzer (WIWEB) and M. Weigand (ZF-L)

After a CH-53D helicopter accident in 2002, a fatigue crack was found in the lower planetary carrier plate of the main rotor gearbox (Figure 2). Due to this accident safety precautions had to be taken to avoid similar accidents in the future.

In cooperation between the German Air Force, ZF and WIWEB the fatigue live of this structure was evaluated, solutions to guarantee the serviceability of the helicopter were established and a new lower planetary carrier plate with an increased fatigue life has been developed (Figure 3).

In order to perform these tasks the following steps were taken:

- evaluation of material properties (quasi-static, fatigue, crack propagation, fracture mechanics) as a basis for further analysis
- first analytical assessment using safe life and damage tolerant concepts
- In-flight measurements at the main rotor shaft during a variety of flight conditions
- finite element modelling of the whole gearbox in order to establish the correct loading situation of the lower planetary carrier plate
- creating a load spectrum representative for the German Air Force
- applying of the above mentioned data and techniques on this load spectrum
- full scale fatigue and crack propagation tests of the lower planetary carrier plate with operational loads on a specially designed test rig including three dimensional strain measurements
- full scale structural tests to evaluate the residual strength of the lower planetary carrier plate with fatigue cracks of different lengths
- evaluation of the critical crack length
- development and verification of a non destructive test method to detect small fatigue cracks
- performing a safety analysis based on the damage tolerance concept in order to predict the fatigue life and establish inspection intervals
- based on the test data and safety analysis a new planetary carrier plate with a strongly increased fatigue life was designed to enable the future service of the helicopter

This investigation shows that an integrated analysis based on a damage tolerance concept, reliable test data and verified non destructive test procedures meets the requirements of the airworthiness regulations as well as the demands for high operational safety and economic efficiency. It is a useful tool for the managing of aging fleets, fatigue life extension and repair solutions.

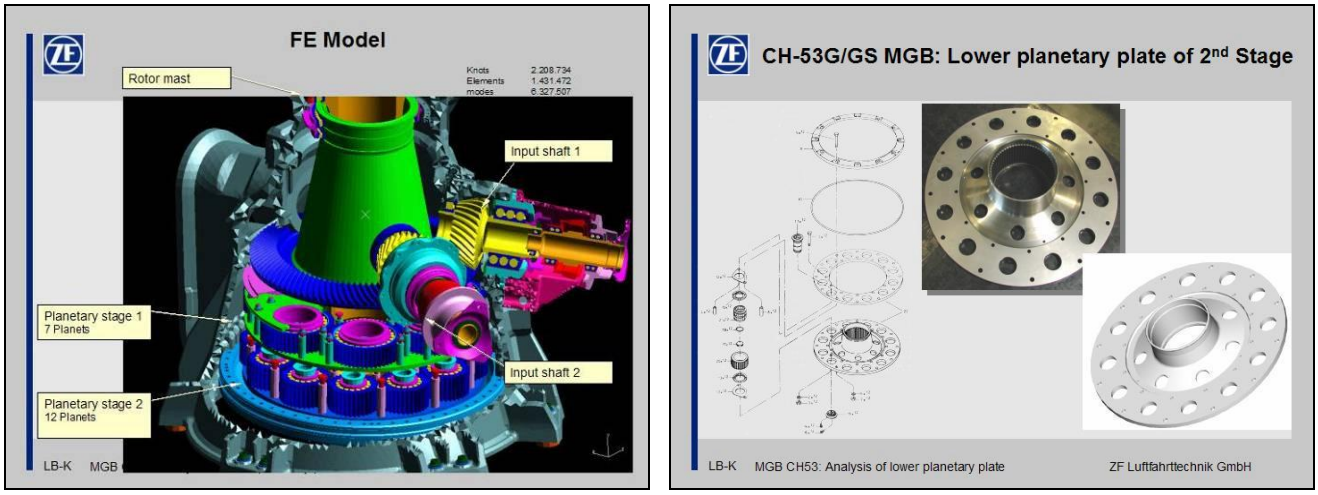

Figure 2 CH-53G: FE-model of the gear box and lower planetary plate

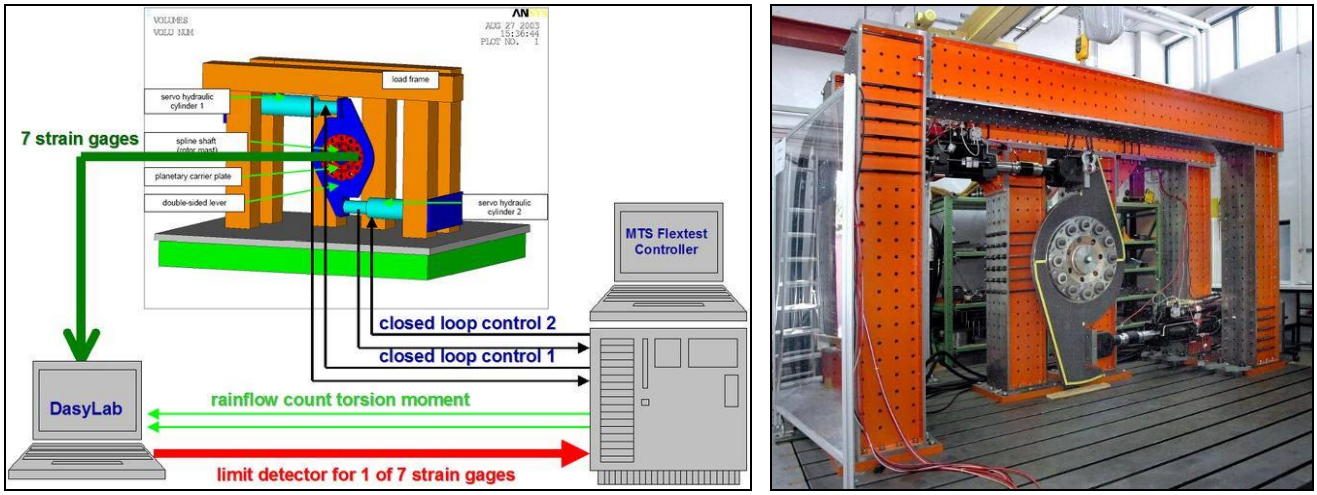

Figure 3 Test set up and test rig for the full scale fatigue tests on the lower planetary plate

2.4 A380 Flap Track No. 6 Static and Fatigue Certification Test and A380 Flap Track No. 3 Fatigue and Damage Tolerance Test

M. Semsch and Th. Grafe (IMA)

A380 flap track tests number 6 (static and fatigue certification) and number 3 (fatigue and damage tolerance) are performed at IMA-Dresden (Figure 4). The objective of the tests is the experimental verification of the static, fatigue and damage tolerance behaviour of the flap tracks. The test program involves assessment of the static strength and fatigue in case of manufacturing defects, artificial damages and repair solutions.

During fatigue testing, simulation of the real flight conditions is done by a realistic load spectrum applied to the structure by ten hydraulic jacks, Figure 5 and Figure 6.

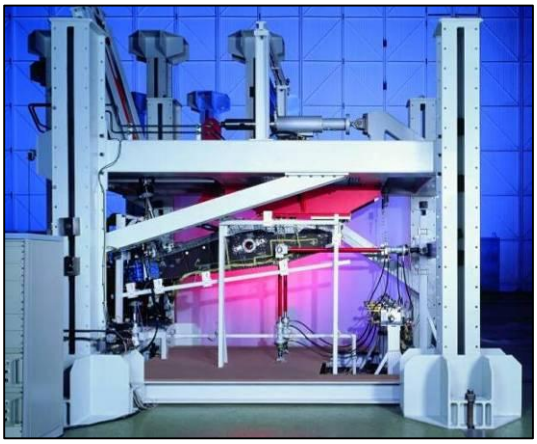

Figure 4 Test rig „A380 Flap Track No.6“

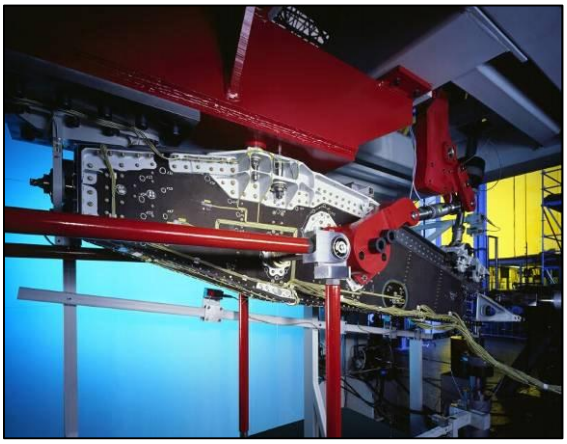

Figure 5 Parts of the track load application

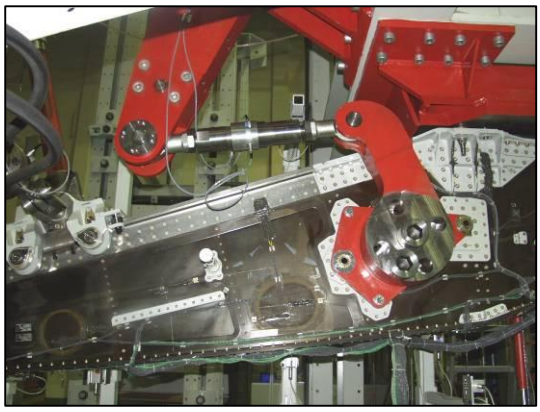

Figure 6 Rotary drive dummy for load introduction in A380 Flap Track Tests

2.5 Fatigue Test of A400M Lug with Bushings

M. Semsch and J. Hornschuh (IMA)

IMA-Dresden performed a fatigue test of A400M lugs with and without bushings. The aim of the tests is the experimental investigation of the influence of special bushings of the fatigue behaviour. The investigations contain tests with constant amplitude and with spectrum loading. The application of bushes is expected to increase the lug’s life cycle.

Figure 7 Lug with bushing

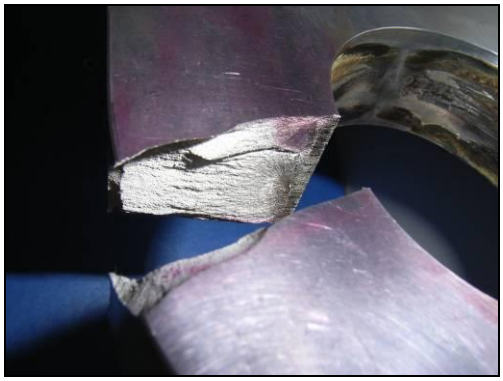

Figure 8 Damaged lug

2.6 Static and dynamic testing of a Flap Rear Link

M. Semsch and T. Alder (IMA)

In the framework of A380 certification a rear link fatigue test was performed. The test procedure covers a rear link with and without artificial damage.

The tests are intended to represent low temperature conditions. In this condition, the ball frictions induce a bending moment, applied by an eccentricity. IMA-Dresden developed a test rig with adjustable eccentricities for load introduction in different directions. This way, the in-plane/out-plane friction moment can be achieved by a single load in a standard test machine (Figure 9).

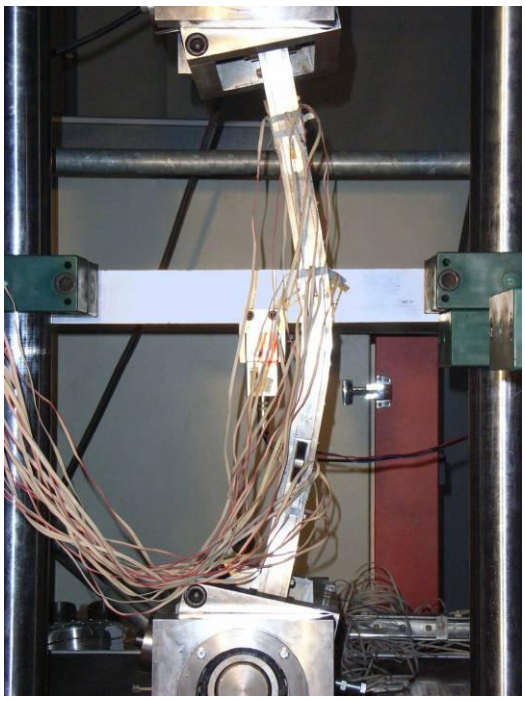

Figure 9 Test set-up under max deflection of the link during a static load case beyond ultimate load

2.7 A380 Torsion Bar Test

D. Melzer and R. Best (IMA)

At IMA–Dresden, a fatigue test of a torsion bar was performed for the certification program of the A380-800 passenger-doors (Figure 10).

Figure 10 Torsion bar, three specimens

The torsion bars were sinusoidal loaded with a pre-load of φ_{min} and a maximum load up to φ_{max} (Figure 11).

The test rig in Figure 12 shows the hydraulic oscillating actuator for the load introduction and the fixed support on the other side.

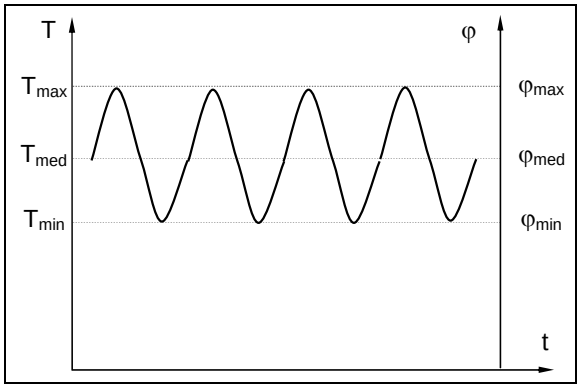

Figure 11 Principle illustration of dynamic tests

Figure 12 Test rig, dynamic

2.8 Static and Fatigue Testing for the Intermediate Casing TP400-D6

R. Best, Th. Grafe, M. Sachse (IMA) and M. Gräber (Rolls-Royce)

The Intermediate Casing (IMC), a major component of the core engine, connects the Intermediate-Pressure Compressor Casing (IPC) with the High-Pressure Compressor Casing (HPC) and is supporting two main engine bearings and the accessory gearbox.

In order to demonstrate this component's compliance with the corresponding certification requirements, the IMC of the Rolls-Royce TP400-D6 was subjected to static and fatigue tests.

A rig test concept has been developed by IMA-Dresden and is shown in Figure 13. In this configuration, the load is applied by hydraulic actuators and the original IPC and HPC are replaced by dummy parts with representative stiffness and strength.

Subsequently, the fatigue tests were performed with load sequences simulating a representative flight load spectrum. The first part of this program covered static limit load and ultimate load cases. The necessary test loads were provided during validation of a whole-engine finite element model, which was another objective of these tests.

Dimensional geometry check-ups and non-destructive testing of the IMC prior to and after subjection to certain load cases were part of the test-program.

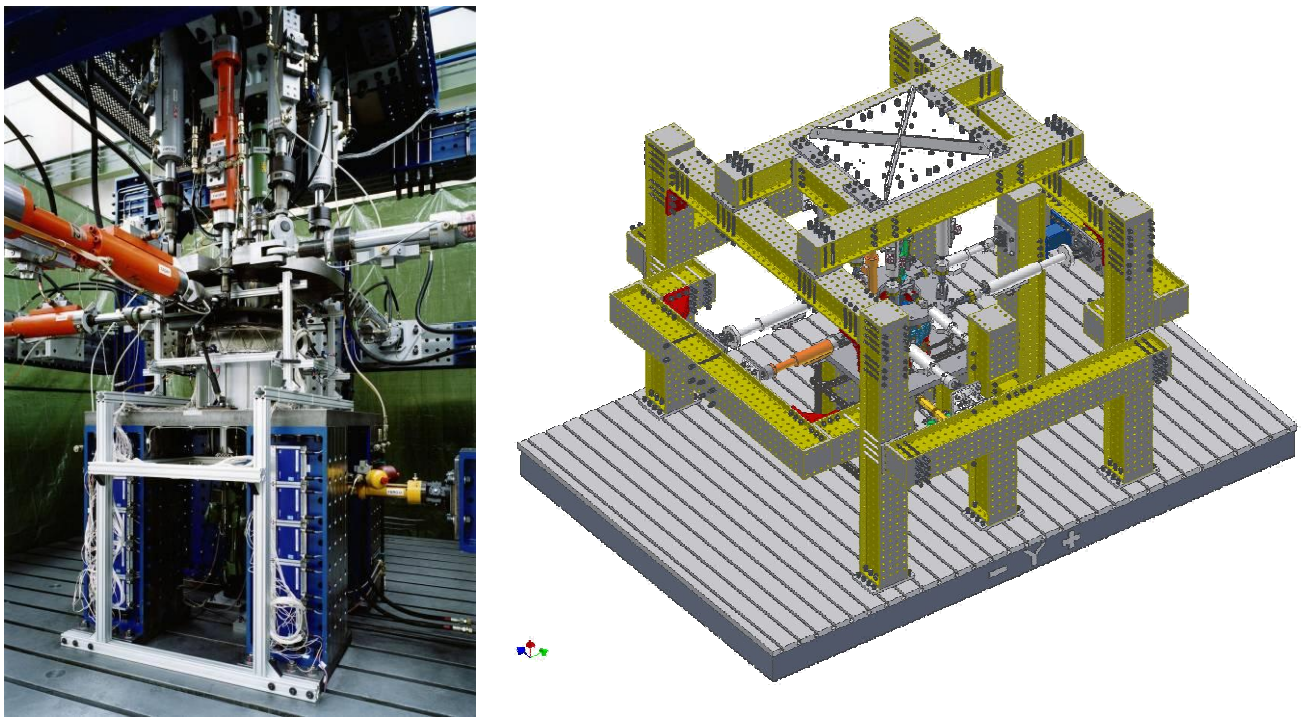

Figure 13 Actual and virtual test set-up at IMA-Dresden

3 Loads

No contributions.

4 Fatigue and Fracture of Fuselage Panels and Joints

4.1 Finite Element Analysis for Advanced Fastened Repair Solutions

D. Furfari (Airbus-D) and G. Schmidt (High-End Engineering on behalf of Airbus)

In the frame of the EU project IARCAS, the fatigue behaviour of advanced repair solutions has been investigated [1]. The operational costs to maintain in-service aircraft, meeting the required levels of safety, rise with increasing time that these planes remain in service [2]. Existing repair solutions, contemplated in the Structural Repair Manual (SRM) of an aircraft, should be improved and developed in order to postpone fatigue crack initiation and extend the crack growth life (i.e. reducing operation costs). The experimental part of this project is described more detailed in a scientific paper [3].

Beside the test activities, calculation methods (based on finite element models) were developed to improve current methods for prediction of the repairs' fatigue behaviour and to optimisation of the design principles of the advanced repair solutions.

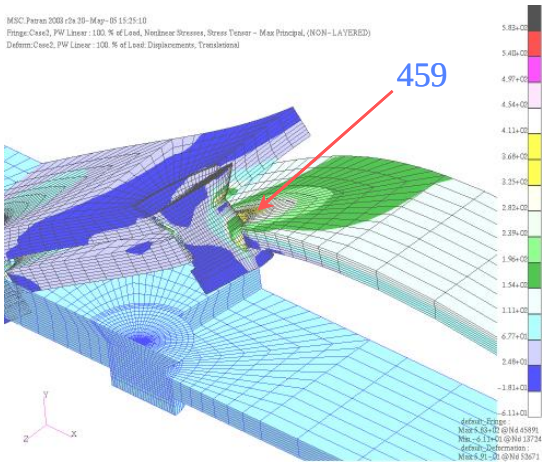

Figure 14 Stress distribution in a 3-D solid model

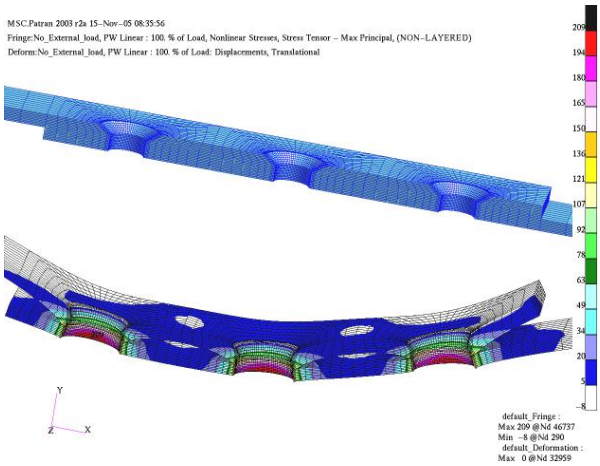

Figure 15 Stress distribution at the minimum stress

For this project, a software tool was developed to study the mechanical behaviour of a flat lap/butt joint under static unidirectional loading. It was used to create the FE models of the advanced riveted repair solution and it consists of several MSC.Patran® macros, that read the input file (.txt file), build the model (including mesh, boundary conditions and load cases) and write an analysis file.

Figure 14 shows an example of the stress distribution using the tool mentioned above. A strip of joint (half rivet pitch) is modelled analysing only solutions where the "full load transfer" condition is respected (e.g. with respect to "coupon specimens" or the middle strip of large repair solution [3]). A detailed 3-D solid model is obtained, including the complete rivet geometry (such as countersunk and formed head). The non-linear GAP elements, as contact definition between the components (all mating surfaces including fastener to surface hole contacts), were used. The GAP element provides point-to-point contact characterisation, setting with different stiffness values both perpendicular and parallel to the contact. The GAP elements are characterised by

four parameters; coefficient of static friction (μ_s), coefficient of kinetic friction (μ_k), initial gap opening (U_0) and preload (F_0). It is possible to simulate the effect of the fastener interference fit by setting an initial value of gap opening or a preload.

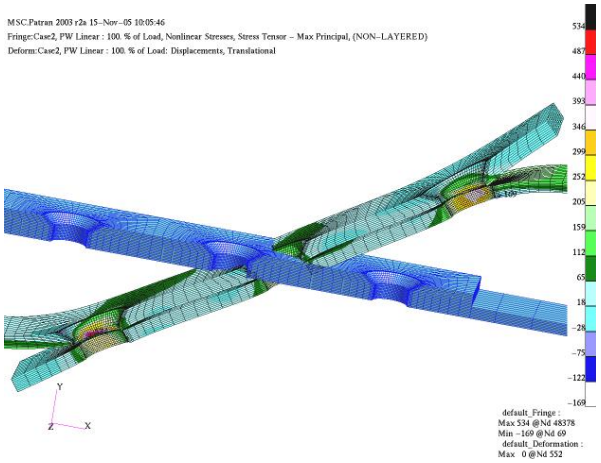

Figure 16 Stress distribution at the maximum stress

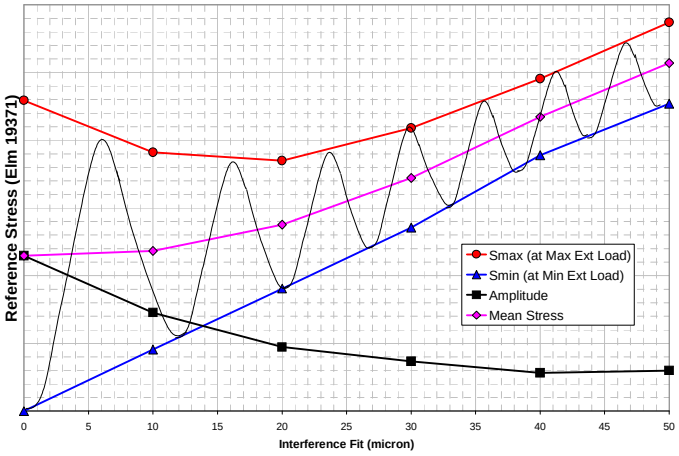

Figure 17 Maximum principal stress distribution at the reference location (Elm 19371 of the FE model)

The interference fit effects (for Hi-Lok fasteners) on the stress distribution of a repair solution with three fastener rows was investigated. The interference conditions are modelled, setting initial values of the gap displacement as described above. The effect of the interference fit on the stress distribution was assessed in terms of σ_{max}, σ_{min}, σ_m (mean stress) and σ_a (stress amplitude) changing. Figure 15 and Figure 16 show the stress distribution at the minimum stress (only due to the interference fit) and the maximum stress (superimposing to the interference fit the external load) respectively. In these figures the fasteners are not shown to highlight the stress concentrations at the fastener holes.

Figure 17 shows the maximum principal stress distribution at the reference location (Elm 19371 of the FE model) of this repair solution for increasing values of interference fit.

The stress shown in the plot is always the maximum principal stress at applied external load (S_{max}), without external load (S_{min}), the resulting amplitude stress $\left(\frac{S_{max} - S_{min}}{2}\right)$ and the mean stress $\left(\frac{S_{max} + S_{min}}{2}\right)$.

The main consequence of an increasing value of the interference fit is the reduction of the amplitude stress, despite of the increasing of the mean stress. For interference values greater than 25-30 μm the effect on the amplitude stress is less significant (horizontal asymptote in the graph).

Fatigue tests on specimens with several grades of IF introduced, demonstrated that fatigue life increases with rising IF values, but no further improvement was found at very high values of IF [3]. This confirms results found with FEA.

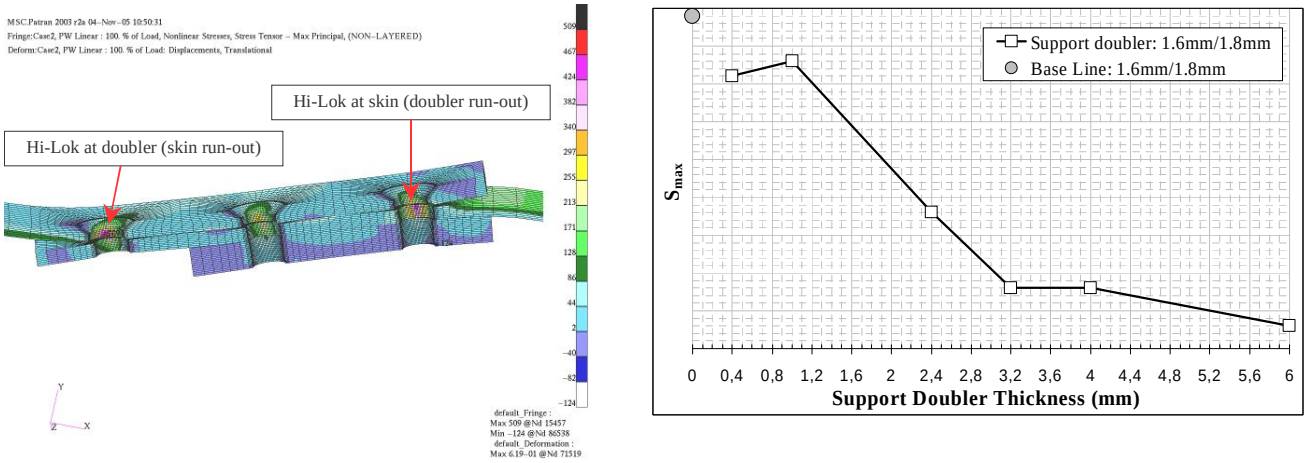

Figure 18 Advanced repair solution "support doubler"

The same software tool was used to optimise the design principles of some repair solutions. For instance in case of the advanced repair solution, called “support doubler” (shown in Figure 18, more details in the related paper [3]) a parametric study has been performed to determine the optimum thickness of the internal additional doubler.

The left hand figure shows the maximum principal stress distribution and the critical location (prone to fatigue crack initiation) in the joint. Also in this case the fasteners were not shown to visualise the peak stress at the critical locations. The stress distribution at these critical locations is affected by the stiffness of the joint. An increase of the support doubler thickness should correspond to an increase of the general stiffness of the joint, which leads to a reduced secondary bending effect with significant reduction of the maximum stress. The increase of the doubler thickness, in fact causes a more pronounced eccentricity effect leading to an increase of the secondary bending. A compromise must be found and the results of this analysis are shown on the right of Figure 18.

[1] Fifth Framework European Project (2000), IARCAS *Improve and Assess Repair Capability of Aircraft Structures, Annex I: Description of the Work*, Contract n^0 G4RD-CT2000-00401, Project n^0 GRD1-2000-25182, coordinated by Airbus-France.

[2] Armstrong A. (2003), In: *Future structures supportability strategy*, Proceedings DSTL Structures Contextual Review.

[3] Furfari D., Meyer C., Lafly A.L., Pramono A. (2007), In *Advanced Repair Design Principles to* Improve *Fatigue and Damage Tolerance Behavior of Fastened Repairs*, to be presented in Proceedings of 24th ICAF Symposium, Naples, Italy.

4.2 Fatigue and Damage Tolerance Test of Fuselage Panels

M. Semsch, A. Keiser and C. Hannemann (IMA)

In the past two years, IMA–Dresden investigated the fatigue and damage tolerance behaviour of several fuselage panels.

For curved, stiffened and pressurised panels, a modular test facility was used, as is shown in Figure 19. With this configuration, A300 and A340 fuselage panels were studied. The system provides three adjustable control channels:

- Internal pressure
- Longitudinal tension load
- Frame loading

IMA-Dresden was in involved in the following projects:

Fatigue tests with artificial scribe marks

In the framework of the "A300 ageing aircraft" program, a fuselage panel cut from a retired aircraft was investigated. The specimen includes a longitudinal lap joint and two fuselage repair solutions.

The fatigue test was performed until fatigue failure. After the initiation of a crack at an artificial scribe mark, the crack propagation was monitored. Additionally, the crack initiation at rivet holes was also focus of this project, Figure 20.

Figure 19 IMA Test facility

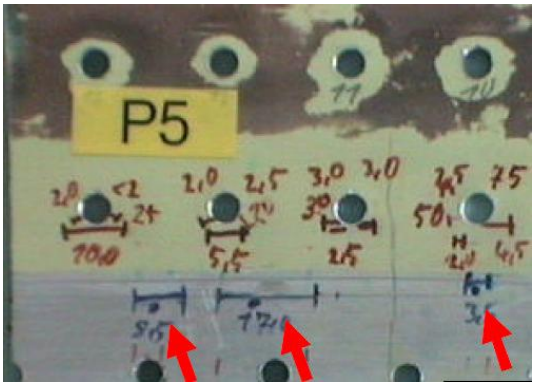

Figure 20 Crack initiation at the lap joint

Fatigue tests of fuselage repair solutions (IARCAS)

In the framework of the IARCAS project, the fatigue behaviour of different fuselage repair solutions was compared.

A repair solution as described in the structural repair manuals was compared to some improved repair proposals. The test was performed until crack initiation. Multiple site cracking occurred at some run outs of riveted repair patches, Figure 21 and Figure 22.

Figure 21 Crack initiation

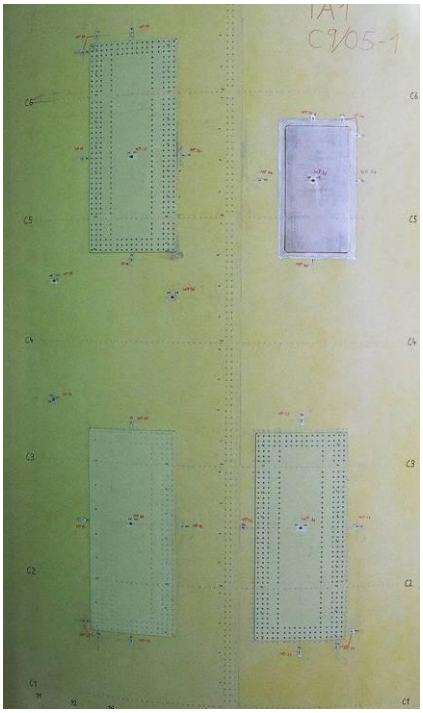

Figure 22 Repair panel

Fatigue and damage tolerance tests of panels with welded stringers

Fatigue and damage tolerance tests were performed on fuselage panels, containing laser beam welded stringers (Figure 23).

Artificial damage was introduced in the weld line by saw cutting. The crack propagation was monitored and finally a residual strength test was performed.

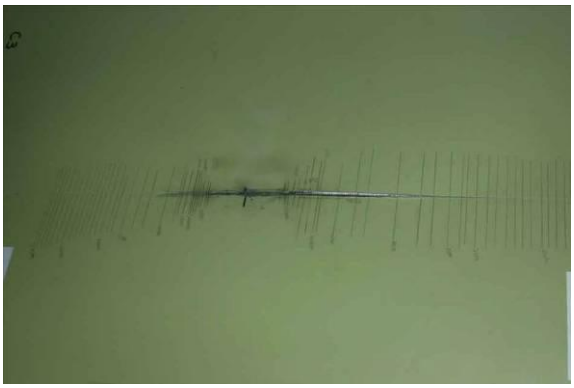

Figure 23 at welded stringer

Figure 24 Panel with FSW joints

Fatigue and damage tolerance tests of panels with FSW joints

This test was performed to investigate the fatigue and damage tolerance behaviour of the friction stir welded (FSW) longitudinal skin joints. An artificially damaged panel with two FSW joints was tested (Figure 24). The crack propagation from the damage was monitored and the residual strength was determined at the end of the test campaign.

4.3 Investigation of Scribe Marks Damages at Fuselage Joints with Finite Element Analysis

D. Furfari, N. Ohrloff (Airbus-D) and G. Schmidt (High-End Engineering on behalf of Airbus)

Depending on the configuration, longitudinal and circumferential fuselage joints may have areas with increased local stresses (in addition to the common locations of high stress concentration, e.g. the rivet holes). This increased stress is caused by the eccentricity of the connected parts which leads to a secondary bending stresses. Damage at the skin surface, which may occur due to standard, in-service maintenance operations (e.g. sealant removal), is critical at these locations as the potential risk of crack initiation is higher due to the higher local stresses.

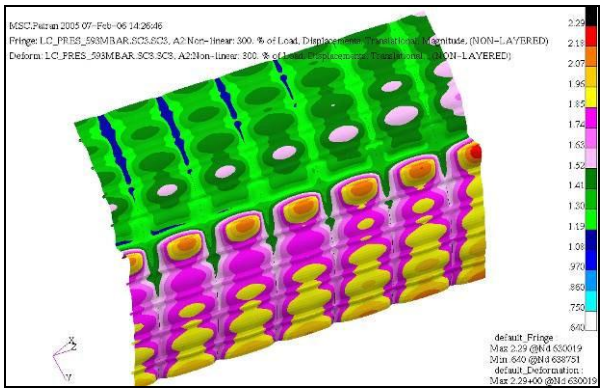

Figure 25 Curved, stiffened panel model

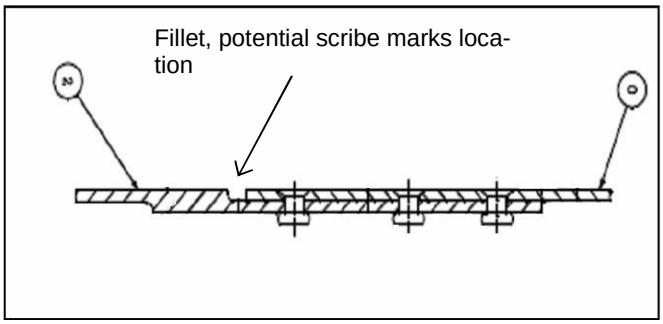

Figure 26 Lap joint with change of skin thickness

To investigate the effect of surface damage near longitudinal joints, several panels with applied artificial scribe marks have been tested [1].

Finite Element (FE) models, able to predict the stresses at the locations with high concentrations, as mentioned above, have been created by means of Patran® Command Language (PCL) macros. Combining the local stress resulted by this FE analysis and analytical approaches (based on linear elastic fracture mechanics theory), the estimation of the fatigue life in presence of scribe marks could be assessed.

Two types of models have been created parametrically: a curved stiffened panel model, build with 2D plate elements (shell elements) and a more detailed model, build with 3D solid elements (brick elements).

Figure 25 shows an example of a curved, stiffened panel model (the deformation under biaxial loading condition, i.e. internal pressure and longitudinal load, is shown in this figure). Frames and stringers as well as fastener connections are also included in the model.

An internal pressure is the applied load together with an axial load (applied in the section at one end of the panel) similar to the one existing in a cylinder as a consequence of the internal pressure applied. The properties of the 2D plate elements used in the model are: thickness, material and offset. The offset definition was used to model the longitudinal joint of the panel because it is important to take the secondary bending effect on the stress distribution at the lap joint into account.

Nonlinear analysis (in terms of large deformations and follower forces) has been performed. A parametric study (by changing the geometry of the panel and/or the joint configuration) could be carried out by using macros, which automatically create the FE models and run the related nonlinear analysis.

Figure 26 shows a lap joint with change in the thickness of the skin. Such a type of joint requires a more detailed 3D solid model to predict the stress distribution in the fillet area, which represents the potential damage location. This type of FE model (a strip of joint, half a rivet pitch wide) can be created with an internal Airbus tool which consists of several MSC.Patran® macros (more details will be presented in the corresponding paper [2]). The modelled area is a strip of the joint including fasteners, but without curvature and stiffeners (i.e. the conservative approach).

The capacity of this type of FE model to estimate secondary bending stresses has been assessed versus strain gauge readings of coupon specimens, containing a step radius at the doubler run out area, with increased bending stress components in this region where the strain gauges were installed.

Figure 27 Test setup of coupon specimens

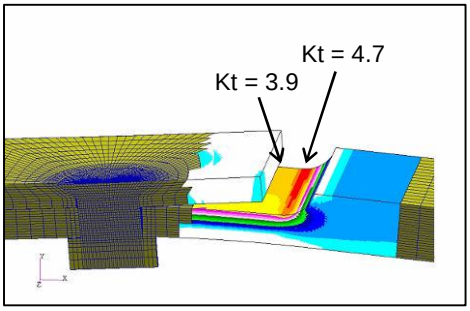

Figure 28 FEA results in terms of K_t

The test setup of this coupon specimen is shown in Figure 27. Strain gauges were placed *back-to-back* in the skin (on the internal and external surface) both in line with the rivet position (position 1 and 3) and at the centreline between two rivets (position 2 and 4).

The next figure (Figure 28) shows the results of the FEA in terms of K_t (stress concentration factor) distribution at the step radius area. The FE model includes GAP elements between fasteners and plates (skin + doubler) to simulate the surface contact (more details in [2]).

The graph in Figure 29 shows *local stresses* vs. *nominal stresses* (stresses are shown in percentage of the stresses applied). The stresses resulted from the FE analysis (thin lines and dots) are compared with the ones measured experimentally by strain gauges (bold lines in the plot).

Stresses predicted with the FE models have shown very accurate values, compared with the ones measured by strain gauges. In particular FE stresses computed in line with fasteners (positions 1 and 3) have shown a relative error below 5%. This error was slightly higher (around 7%) for the stress measurements in the middle pitch of the fastener (positions 2 and 4).

The stresses due to the secondary bending, being evident from the the *back-to-back* placed strain gauges, was well predicted by the FE model.

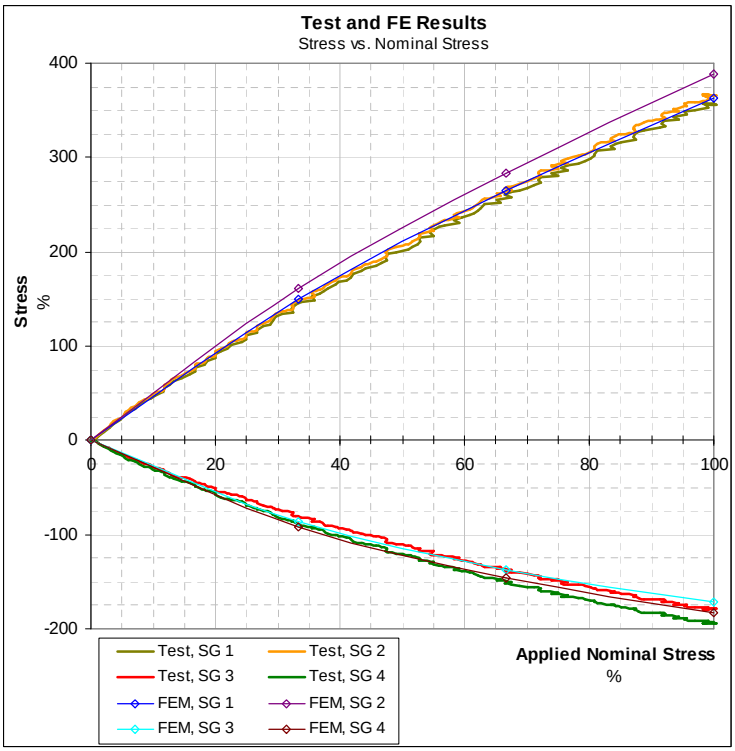

Figure 29 Local stresses vs. nominal stresses

[1] Semsch M., Keiser A., Hannemann C. (2007), In *Fatigue and Damage Tolerance Tests of* Fuselage *Panels*, to be presented as National Review Germany in Proceedings of 24th ICAF Symposium, Naples, Italy

[2] Furfari D., Schmidt G. (2007), In *Finite Element Analysis for Advanced Fastened Repair Solutions*, to be presented as National Review Germany in Proceedings of 24th ICAF Symposium, Naples, Italy

4.4 Discretization Errors by Determining Area, Volume, and Mass Moments of Inertia

L. G. Gelimson (RUAG)

By calculating area, volume, and/or mass and moments of inertia, integration provides the exactness of their values. Discretising the areas, volumes, and/or masses and choosing suitable approximations to them and to the coordinates of their *centroids* (centres of area/volume/mass/gravity) lead to discretisation errors to be estimated.

Consider that it is possible to provide an approximation error as small as required by suitably triangulating each area practically relevant even by using right triangles only whose each cathetus is parallel to one of the axes. Hence it is sufficient to consider the area moments of inertia only of such a triangle with constant thickness. By three-dimensional objects with variable thickness, simply use such triangular ”sheets” whose numbers vary along conventional lengths and/or widths.

To show result invariance by changing the position of such a right triangle, consider a coordinate system one of whose axes contains one cathetus, the hypotenuse dividing the first quad-

rant at the system origin, as well as the central coordinate system with the axes parallel to the above ones. To obtain the lower and upper bound of the order of the corresponding discretisation errors, subsequently choose all the approximations from below and above, respectively. Adding an adjacent rectangle to such a right triangle brings no additional absolute error and therefore decreases the relative error and provides strong estimates.

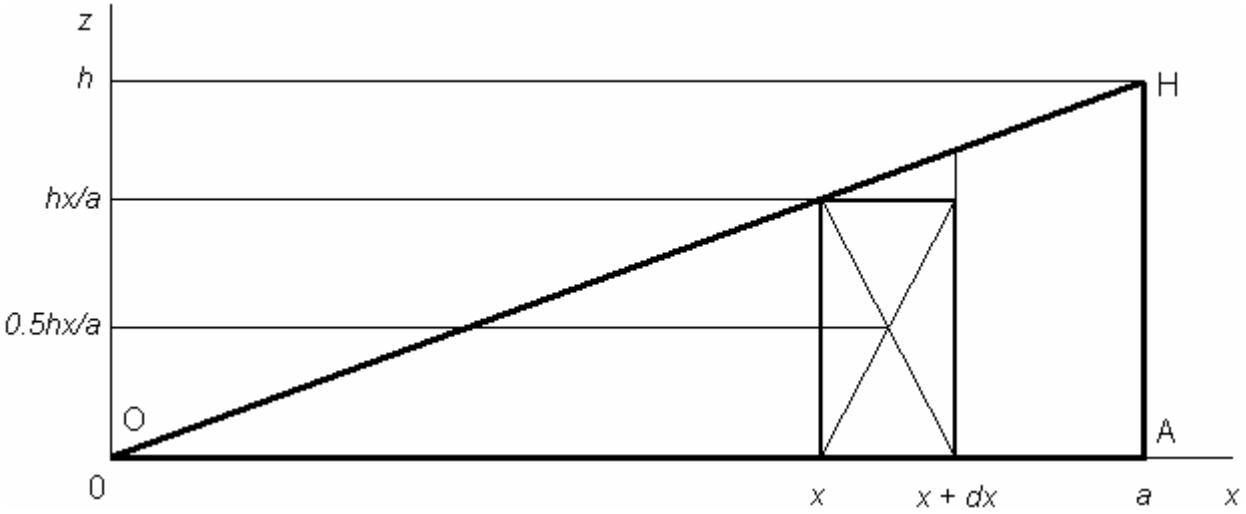

Here *dx* denotes the differential of *x*. For the area moments of inertia I_x and I_z of right triangle OAH with base *a* and height *h* about axes *0x* and *0z*, integration [1] brings the exact results:

$I_x = \int_0^a (hxdx/a)\,(0.5\,hx/a)^2 = 0.25\,h^3/a^3 \int_0^a x^3\,dx = ah^3/16,$

$I_z = \int_0^a (hxdx/a)\,x^2 = h/a \int_0^a x^3\,dx = a^3h/4.$

In a similar figure (not shown) for lower-bound estimating discretisation error, the symbol *n* denotes the (finite) cardinal number of the parts of side OA and thus of the right triangle OAH due to the corresponding vertical lines whereas *k* varies from 0 to *n* – 1, indicating the ordinal number of the part containing the interval between *ak/n* and *a*(*k* + 1)/*n*. Replace the area of the *k*th (trapezoidal) part with the smaller rectangle, take the (smaller) ordinate of the rectangle centroid by calculating I_x , and replace the abscissa of the rectangle centroid with the smaller value *ak*/*n* by calculating I_z . Direct summation brings the following lower-bound estimates:

$I_x = \sum_0^{n-1}(a/n)(hk/n)(0.5hk/n)^2 = 0.25ah^3/n^4\sum_0^{n-1}k^3 = 0.25\,ah^3/n^4\,((n\text{-}1)n/2)^2 = (1\text{-}1/n)^2\,ah^3/16,$

$I_z = \sum_0^{n-1}(a/n)(hk/n)(ak/n)^2 = a^3h/n^4\,\sum_0^{n-1}k^3 = a^3h/n^4\,((n-1)n/2)^2 = (1-1/n)^2\,a^3h/4$

with multiplying their exact values by $(1 - 1/n)^2 = 1 - 2/n + 1/n^2$.

By *n* great enough (e.g. 100 by the order of value), $1/n^2$ is very small and can be omitted. In such a case the factor is about 1 - 2/*n* and the relative error is about 2/*n*, as well as by central axes.

By upper-bound estimating discretisation error, replace the area of the *k*th (trapezoidal) part with the greater (shown) rectangle, take the greater ordinate of the rectangle centroid by calculating I_x , and replace the abscissa of the rectangle centroid with the greater value *a*(*k* + 1)/*n* by calculating I_z . Then direct summation brings the following upper-bound estimates:

$I_x = \sum_0^{n-1} (a/n)(h(k+1)/n)(0.5\, h(k+1)/n)^2 = 0.25\, ah^3/n^4 \sum_0^{n-1} (k+1)^3 = (1+1/n)^2\, ah^3/16,$

$I_z = \sum_0^{n-1} (a/n)(h(k+1)/n)(a(k+1)/n)^2 = a^3h/n^4 \sum_0^{n-1} (k+1)^3 = a^3h/n^4 (n(n+1)/2)^2 = (1+1/n)^2\, a^3h/4$

with multiplying their exact values by $(1 + 1/n)^2 = 1 + 2/n + 1/n^2$. By n great enough (e.g. 100 by the order of value), $1/n^2$ is very small and can be omitted. In such a case the factor is about $1 + 2/n$ and the relative error is about $2/n$, as well as by central axes. We see this value is universal. By three-dimensional discretising (with n_1, n_2, and n_3 great enough, e.g. 100 by the order of value) the object to be considered, the relative error is about $2(1/n_1 + 1/n_2 + 1/n_3)$ and this value is universal, too. Hence by estimating area, volume, and mass moments of inertia [2-4] about both central and non-central axes with using adequate discretisation of objects, any method of reasonably choosing the values of the areas, volumes, and masses of elements, as well as the coordinates of their centroids, leads to results with relative errors small enough.

[3] Encyclopaedia of Mathematics. Ed. M. Hazewinkel. Vols. 1 to 10. Kluwer Academic Publ., Dordrecht, 1988-1994

[4] Handbuch Struktur-Berechnung. Prof. Dr.-Ing. L. Schwarmann. Industrie-Ausschuss-Struktur-Berechnungsunterlagen, Bremen, 1998

[5] Gelimson, L. G.: Elastic Mathematics. General Strength Theory. The ”Collegium” International Academy of Sciences Publishers, Munich (Germany), 2004

[6] Elementos de resistencia de materiales; por S. P. Timoshenko y D. H. Young; traducción de Jesús Ibáñez Gar. 2ª ed. Barcelona: Montaner y Simón, DL 1979

4.5 General Bearing Strength Theory

L. G. Gelimson (RUAG)

Common bearing strength theory [1, 2] regards the only bearing stress in a complex three-dimensional stress state at a point under consideration and only selected values of the e/a ratio, namely 4 and 3, with linearly interpolating between them, declaring the necessity of special investigations between 3 and 2, and forbidding any values less than 2, see Figure 30.

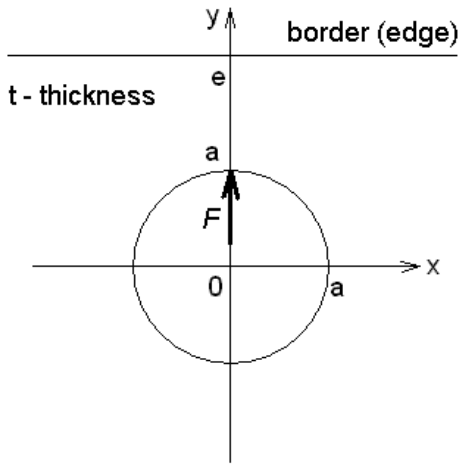

Figure 30 Schematical plate with hole and acting force

A plate has thickness *t* and a round hole of radius *a* with minimum distance *e* from the hole center to the border (edge) of the plate. Force *F* acts on the point (0, *a*) normally to the border (edge) of the plate. By elasticity, elastic contact theory could be used. By plasticity, at the point (0, *a*), the modulus (absolute value) of the average radial stress $\sigma_r = -F/(2at)$ plays the bearing role and should be compared with the traditional bearing strength [1, 2].

The average shear stress $\tau = F/(2et)$. But the real distribution of τ is nonhomogeneous – theoretically vanishing at the ends and maximum in the middle [3]. By the parabolic distribution [3] of τ, its maximum is the above average value multiplied by 1.5, by stepwise linear distribution – multiplied by 2. To be conservative, take factor 2 the greatest among the both. Then $\tau = F/(et)$. However, such values of τ can hold by $x = a$ and $x = -a$ but not by $x = 0$. Therefore, by determining the equivalent stress at the point (0, *a*), we take $\tau = 0$ assuming symmetricity by the y axis and no friction. The maximum tangential stress by elasticity

$$\sigma_t = F / (2at) * (e^2 + a^2) / (e^2 - a^2)$$

holds at the point (0, *a*) by the Lame formulae. By plasticity, the maximum tangential stress holds at the point (0, *e*) with vanishing the radial stress σ_r. Therefore, it is conservative to consider the point (0, *a*) with the real radial stress whose modulus (absolute value) achieves its maximum and with the average tangential stress

$$\sigma_t = F / (2at) * a / (e - a) = F / [2(e - a)t]$$

by the equilibrium condition like that by a cylindrical shell. The remaining normal (axial) stress σ_z vanishes: $\sigma_z = 0$. The corresponding pure (dimensionless) stresses at the point (0, *a*) in general strength theory [3] are

$$\sigma^\circ_r = \sigma_r / \sigma_{LB} = -F/(2at\sigma_{LB}),\ \tau^\circ = \tau / R_m = 0,$$
$$\sigma^\circ_t = \sigma_t / R_m = F / [2(e - a)t\, R_m],\ \sigma^\circ_z = \sigma_z / R_m = 0.$$

Here Rm is the ultimate strength by tension, σLB the ultimate bearing strength [2],

$$\sigma^\circ_r = \sigma_r / \sigma_{LB},\ \tau^\circ = \tau / R_m,\ \sigma^\circ_t = \sigma_t / R_m,\ \sigma^\circ_z = \sigma_z / R_m$$

with a little circle on the right-hand side above are the corresponding pure (dimensionless) stresses in general strength theory [3] obtained from the usual ones by dividing them by their uniaxial ultimate values in the same direction with the same sign, τ being divided by the ultimate normal stress to conserve the form of a critical strength criterion generalizing the Huber-von Mises-Henky criterion where the factor by each τ^2 is the factor by each σ^2 multiplied by 3. Dividing τ by τ_u (the ultimate shear stress) with replacing this factor 3 by 1 would give the same result but the criterion formula for the pure (dimensionless) stresses would be not similar to the criterion formula for the usual stresses. The pure (dimensionless) equivalent stress σ°_e at the point

(0, a) in general strength theory [3] correcting and generalizing many known criteria, too, and the reserve factor [3] *n* are

$$\sigma^\circ_e = (\sigma^\circ_t{}^2 - \sigma^\circ_t \sigma^\circ_r + \sigma^\circ_r{}^2 + 3\,\tau^{\circ\,2})^{1/2} =$$

$$F/(2at\,R_m) * [a^2/(e - a)^2 + a/(e - a) * R_m/\sigma_{LB} + (R_m/\sigma_{LB})^2]^{1/2},$$

$$n = 1/\sigma^\circ_e = 2at\,R_m/\,F\,/\,[a^2/(e - a)^2 + a/(e - a) * R_m/\sigma_{LB} + (R_m/\sigma_{LB})^2]^{1/2}.$$

[1] Military Handbook. Metallic Materials and Elements for Aerospace Vehicle Structures. MIL-HDBK-5H, 1998
[2] Handbuch Struktur-Berechnung. Prof. Dr.-Ing. L. Schwarmann. Industrie-Ausschuss-Struktur-Berechnungsunterlagen, Bremen, 1998
[3] Gelimson, L. G.: Elastic Mathematics. General Strength Theory. The "Collegium" International Academy of Sciences Publishers, Munich (Germany), 2004

4.6 General Bearing Strength Theory by Replacing Plate Parts with Washers

L. G. Gelimson (RUAG)

The present work is dedicated to further extending general bearing strength theory [1] by introducing washers between sheets and fasteners, e.g., by corrosion in the plate about the hole, is removing some ring $a \le r \le b$ (see Figure 31) with most corrosion, removing the remaining corrosion by $r \ge b$, and then placing a new, specially manufactured ring $a \le r \le b$ with the initial thickness t_{max}:

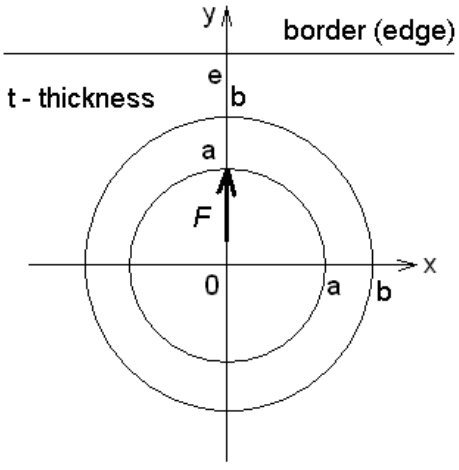

Figure 31 Schematical plate with acting force

In this case, the stress states at the both points (0, *a*) of the washer and (0, *b*) of the hole should be considered. Analogously to [1], in the washer, the maximum shear stress

$$\tau_a = [F\,/\,(2at) * 2at - F\,/\,(2bt) * 2at]\,/[(b^2 - a^2)^{1/2}\,t] = F/(bt) * [(b - a)/(b + a)]^{1/2}.$$

However, such values of τ can hold by $x = a$ and $x = -a$ but not by $x = 0$. Therefore, by determining the equivalent stress at the point (0, a), we take $\tau = 0$ assuming symmetricity by the y axis and no friction. The normal (axial) stress σ_z vanishes: $\sigma_z = 0$. The average tangential stress

$$\sigma_{ta} = [F / (2at) - F / (2bt)] * a / (b - a) = F / (2at) * (1 - a/b) * a / (b - a) = F / (2bt).$$

The corresponding pure (dimensionless) stresses in general strength theory [4] are

$$\sigma^\circ_r = \sigma_r / \sigma_{LB} = -F/(2at\sigma_{LB}),\ \tau^\circ = \tau / R_m = 0,$$
$$\sigma^\circ_t = \sigma_t / R_m = F / [2btR_m],\ \sigma^\circ_z = \sigma_z / R_m = 0.$$

The pure (dimensionless) equivalent stress at the point (0, a) in general strength theory [4] and the reserve factor are

$$\sigma^\circ_e = (\sigma^{\circ\,2}_t - \sigma^\circ_t \sigma^\circ_r + \sigma^{\circ\,2}_r + 3\,\tau^{\circ\,2})^{1/2} = F/(2atR_m) * [(a/b)^2 + a/b * R_m/\sigma_{LB} + (R_m/\sigma_{LB})^2]^{1/2},$$
$$n = \text{R.F.} = 1/\sigma^\circ_e = 2atR_m / F / [(a/b)^2 + a/b * R_m/\sigma_{LB} + (R_m/\sigma_{LB})^2]^{1/2}.$$

By $r \geq b$, the minimum thickness $t_{min\,b} \geq t_{min}$ and, to be conservative, namely $t_{min\,b}$ should be used instead of t. For the plate strength at the point (0, b) the average radial stress $\sigma_{rb} = -F/(2bt_{min\,b})$, and the maximum shear stress $\tau = F/(et)$.

However, such values of τ can hold by $x = b$ and $x = -b$ but not by $x = 0$. Therefore, by determining the equivalent stress at the point (0, b), we take $\tau = 0$ assuming symmetricity by the y axis and no friction. The normal (axial) stress σ_z vanishes: $\sigma_z = 0$. The average tangential stress

$$\sigma_t = F / (2bt) * (e + b) / 2 / (e - b) = F * (e + b) / [4b(e - b)t].$$

The pure (dimensionless) stresses at the point (0, b) in general strength theory [4] are

$$\sigma^\circ_r = \sigma_r / \sigma_{LB} = -F/(2bt\sigma_{LB}),\ \tau^\circ = \tau / R_m = 0,$$
$$\sigma^\circ_t = \sigma_t / R_m = F * (e + b) / [4b(e - b)tR_m],\ \sigma^\circ_z = \sigma_z / R_m = 0.$$

The pure (dimensionless) equivalent stress at the point (0, b) in general strength theory [4] and the reserve factor are

$$\sigma^\circ_e = (\sigma^{\circ\,2}_t - \sigma^\circ_t \sigma^\circ_r + \sigma^{\circ\,2}_r + 3\,\tau^{\circ\,2})^{1/2} =$$
$$F/(2btR_m) * \{[(e + b)/2/(e - a)]^2 + (e + b)/2/(e - a) * R_m/\sigma_{LB} + (R_m/\sigma_{LB})^2\}^{1/2},$$
$$n = \text{R.F.} = 1/\sigma^\circ_e = 2btR_m / F / \{[(e + b)/2/(e - a)]^2 + (e + b)/2/(e - a) * R_m/\sigma_{LB} + (R_m/\sigma_{LB})^2\}^{1/2}.$$

Many comparisons have shown that general bearing strength theory gives results similar to those of the lug model and unlike it, provides investigating washer strengths and optimizing the choice of washer geometry and material by considering different possibilities.

[1] Gelimson, L. G.: General Bearing Strength Theory. In: Review of Aeronautical Fatigue Investigations in Germany During the Period 2005 to 2007, Dr. Claudio Dalle Donne, EADS Corporate Research Center Germany
[2] Military Handbook. Metallic Materials and Elements for Aerospace Vehicle Structures. MIL-HDBK-5H, 1998
[3] Handbuch Struktur-Berechnung. Prof. Dr.-Ing. L. Schwarmann. Industrie-Ausschuss-Struktur-Berechnungsunterlagen, Bremen, 1998
[4] Gelimson, L. G.: Elastic Mathematics. General Strength Theory. The ”Collegium” International Academy of Sciences Publishers, Munich (Germany), 2004

5 Fatigue and Fracture of Integral Panels and Welded Joints

5.1 Integral Structure – Welding of Clips – Design Optimization

S. Werner and N. Ohrloff (Airbus-D)

Whereas the welding of stringers has been introduced in nearly all aircraft programmes of Airbus, the clips – the connection between the skin and the frame – are still riveted. The reason was the poor fatigue behaviour of the start and the stop of the weld line acting like a sharp notch.

In a second approach an extensive study based on finite element method (FEM) and strain gauge measurement led to a design optimization. Moreover, a simple coupon combined with an appropriate clamping has been derived from this study, Figure 32. The coupon has to show the same stress distribution in the skin and in the clip (respectively the shear web) like in the real aircraft structure.

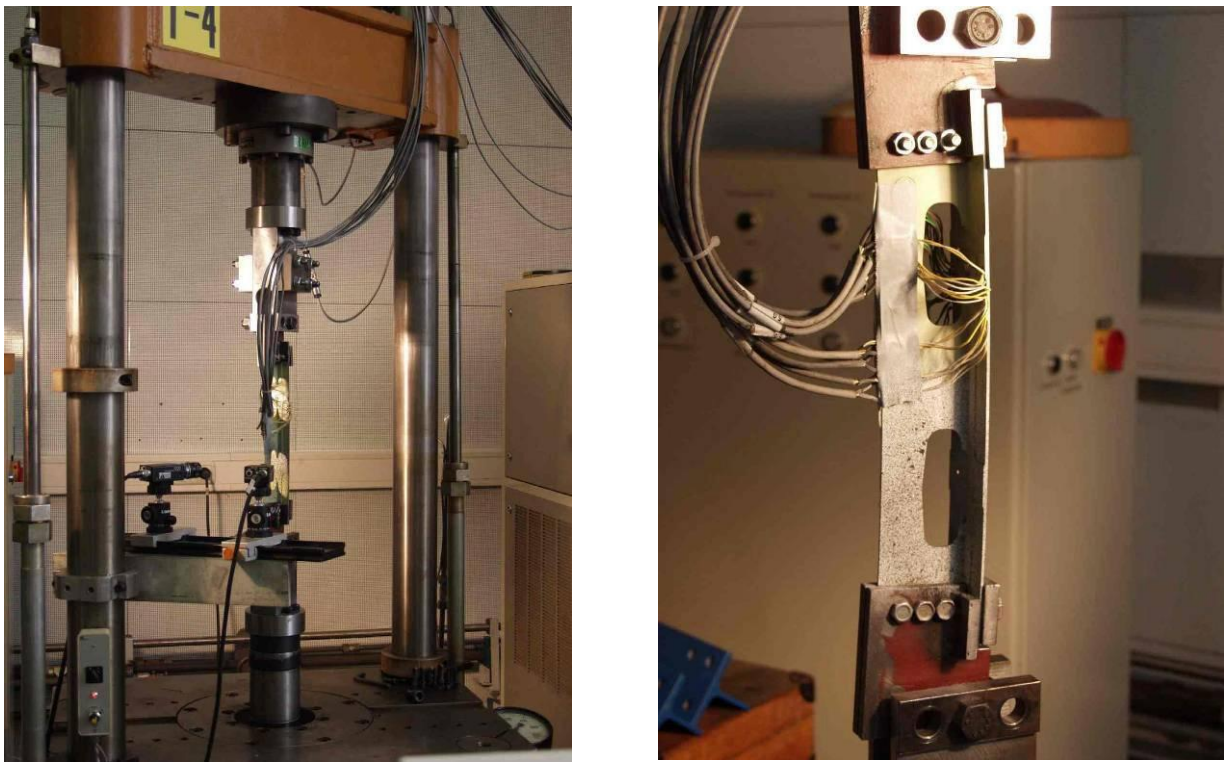

Figure 32 Clip welding - coupon in the test rig

With this coupon the former design solution was tested at first to get a relation to the known full scale fatigue test results. Afterwards, the fatigue behaviour of the optimized design was determined. Finally, the design solutions showing a satisfying result will be tested in full scale (curved pressurized panel with all stiffening elements).

Not forgetting the damage tolerance behaviour, the integral structure with added welded clips has to prove its strength in the presents of long cracks also (large damage capability).

This exercise shows the importance to have a representative coupon and a reliable FEM model for the phase of design optimization.

5.2 Biaxial Fatigue of Friction Stir and Laser Beam Welded Stiffened Panels

J. Schneider, C. Sick, K.-H. Trautmann and G. Biallas (DLR)

Within the framework of the European WelAir (development of short distance WELding concepts for AIRframes) project, a method to fabricate cruciform specimens from stiffened components has been established. Cruciform specimens were made from both FSW overlap T-joints produced by EADS in Suresnes and LBW T-joints delivered by Alenia. The specimens could be fatigued in the relevant 50000 to 100000 number of cycles to failure regime, if a maximum stress of 100 MPa and a stress ratio R of 0.1 was applied. To further resemble the biaxial loading situation of stiffened fuselage structures, the cruciform specimens were loaded proportionally without any phase shift, but with different load ratios λ between the loading components in both directions.

For single-stringer panels, natural crack initiation and subsequent crack growth were governed by the sharp stiffness gradient caused by introducing the stringer irrespective of the welding process applied. Cracks initiated and propagated at run-in and run-out locations in a direction perpendicular to the weld seam. The shortest fatigue life was observed for uniaxial loading in stringer direction (λ = 0). An additional stress component perpendicular to the joint line (λ > 0) reduced deformation in welding direction before crack initiation and diminished crack opening at maximum load after crack initiation both resulting in a higher number of cycles to failure. Characteristics of a crack propagating from a saw-cut along the weld seam were not markedly deteriorated as compared to crack growth in the base material.

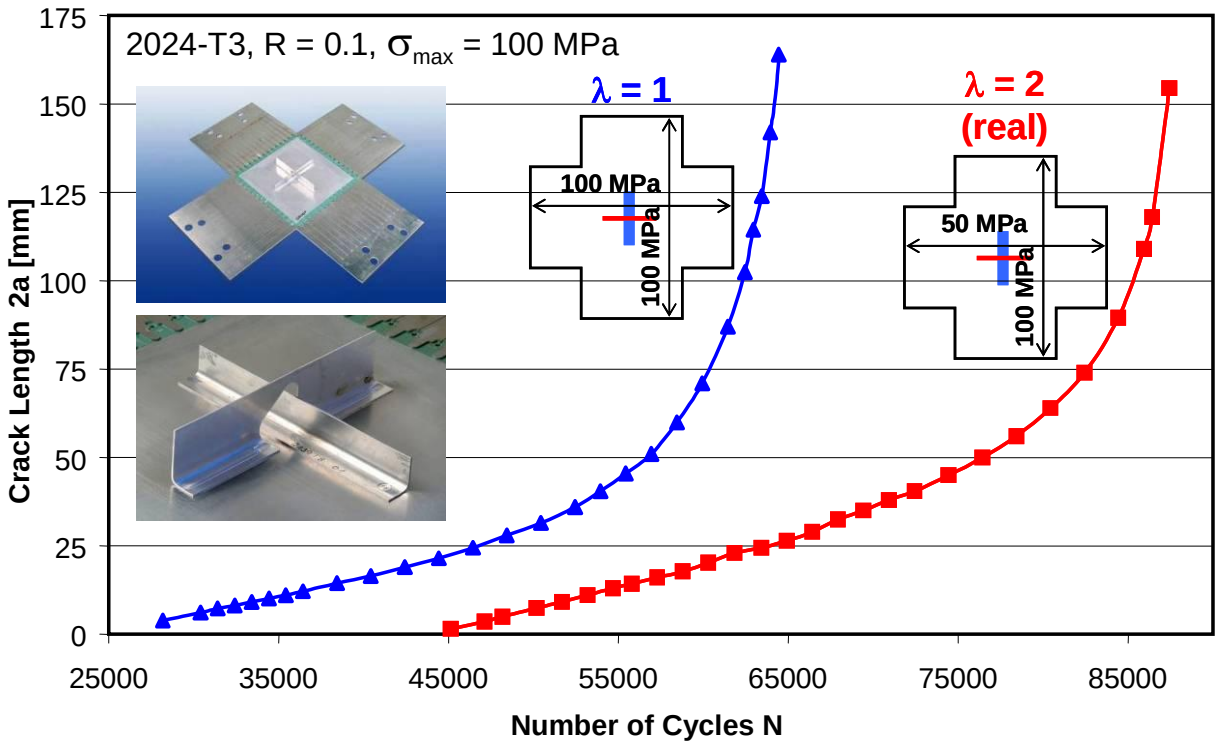

Figure 33 Fatal crack length at stringer (λ = 1) / at clip (λ = 2) for FSW stringer-frame panels made exclusively from 2024-T3

However, depending on the load component perpendicular to the joint line, crack growth from the saw-cut competed with the growth of cracks initiated naturally at run-in and run-out locations.

The insets in Figure 33 are depicting the FSW clip-stringer configuration investigated. A variety of cracks could be observed on specimen back side of those panels (Figure 34). In the course of the test for $\lambda = 1$, the crack at the beginning of the stringer turned out to become the fatal one. For the sake of clarity, only data of the respective fatal crack are shown Figure 33. Similar to single-stringer panels, increasing the load ratio λ also increased the number of cycles to failure for FSW stringer-frame structural members (Figure 33), but additionally gives a different location of the fatal crack. Figure 34 illustrates that the fatal crack changed from stringer ($\lambda = 1$) to frame ($\lambda = 2$). The load ratio λ of 2 is labelled real in Figure 33 and Figure 34 since it resembles quite closely the loading situation of stringer-frame structural members in upper sections of a pressurized fuselage.

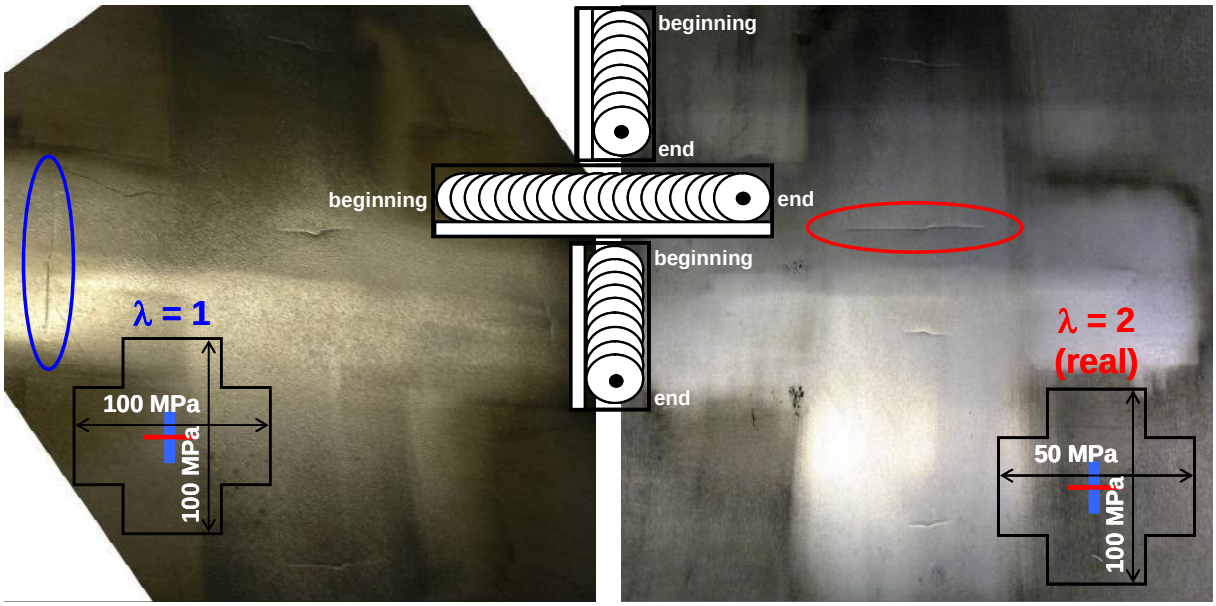

Figure 34 Cracks at beginning/end of seam observed on specimen back side (FSW stringer-frame panels made exclusively from 2024-T3, fatal cracks are highlighted)

When the frame of a FSW stringer-frame panel made exclusively from 2139-T8 was replaced by a high-strength PA765-T79 frame, crack growth behaviour was slightly improved. However, the crack growth characteristics of this 2139-T8 skin and stringer / PA765-T79 frame panel were still not better than those of a panel made exclusively from 2024-T3.

5.3 Stress Intensity Factors due to Welding Residual Stresses Determined by Cut-Compliance Measurements

K. Zimmermann and G. Biallas (DLR)

It is well known that residual stresses have a strong impact on crack growth behaviour of friction stir welded (FSW) joints especially for lower R ratios and lower stress intensities. To investigate the effect of welding process parameters on residual stresses, FSW butt joints were made from

2024 material at a constant rotational speed of 850 rpm and two different welding speeds of 100 or 400 mm/min, respectively. The stress intensity factor due to welding residual stresses K_{rs} was directly determined by the cut-compliance method [1-3]. The method is based on the crack compliance method: a narrow saw cut is introduced progressively into the potential crack plane of the considered CT specimen (or any other component) and the resulting strain change is measured by a strain gauge (see inset in Figure 35). The desired stress intensity factor is proportional to the slope of the measured strain ε plotted as a function of the cut depth a. The cut-compliance method delivers the specimen response on residual stresses in a form suitable for direct use in the fracture mechanical characterization of crack growth. Moreover, the elastic redistribution of residual stresses with increasing crack length is implicitly included in the K_{rs} versus a solution [3].

In Figure 35 it is illustrated that a higher welding speed increased the amount of both tensile and compressive K_{rs}, whereas the distance between maximum and minimum K_{rs} is reduced. Nevertheless, the amount of compressive K_{rs} in front of the joint line is still considerable for the lower welding speed and can not be neglected, if crack growth rates in the Paris regime have to be analysed. The good reproducibility of cut-compliance measurements is demonstrated by duplicate measurements for both welding conditions.

The calculation of the underlying residual stress distribution in the un-cracked structure by the weight function method is not straightforward. The residual stress recalculation procedure for CT specimens used in Figure 36 has been described in [4], and it has been shown that the resulting residual stress distributions are in good qualitative and quantitative agreement with

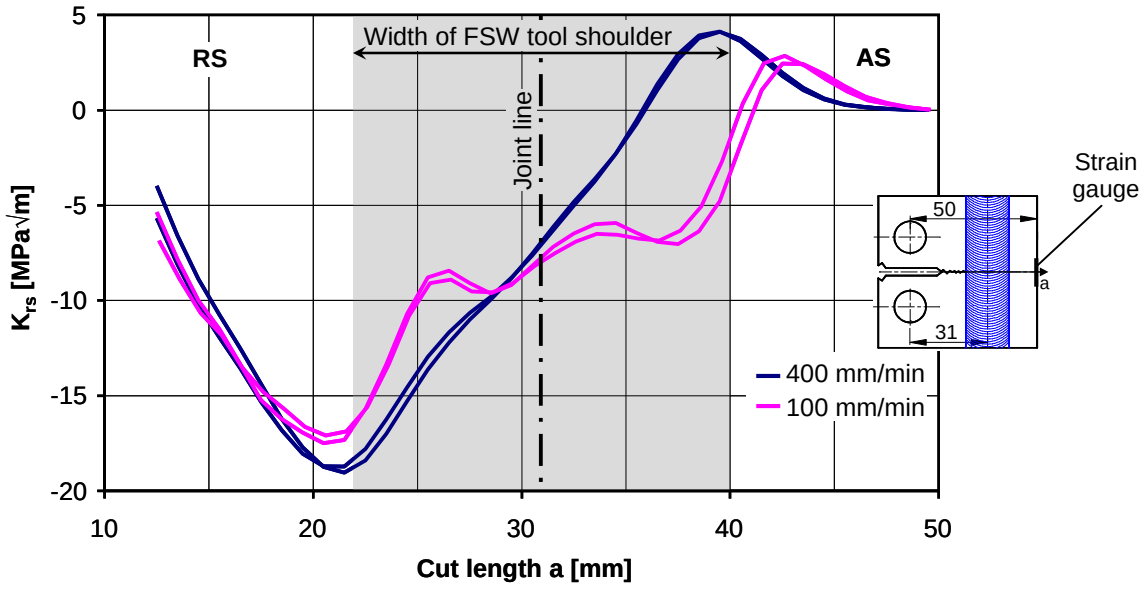

Figure 35 Distribution of K_{rs} in transverse CT specimens measured by the cut compliance method

those determined by different diffraction methods. In addition to Figure 35, Figure 36 reveals that the zone of tensile residual stresses is more concentrated to the weld centre if a higher welding speed is applied. Note that, contrarily to the tensile residual stresses dominating Figure 36, negative stress intensity factors K_{rs} were mainly acting at the crack tip in Figure 35. Obviously, the residual stresses redistributed in such a way that compressive stresses were maintained at the crack tip over a long period of crack growth especially for the lower welding speed.

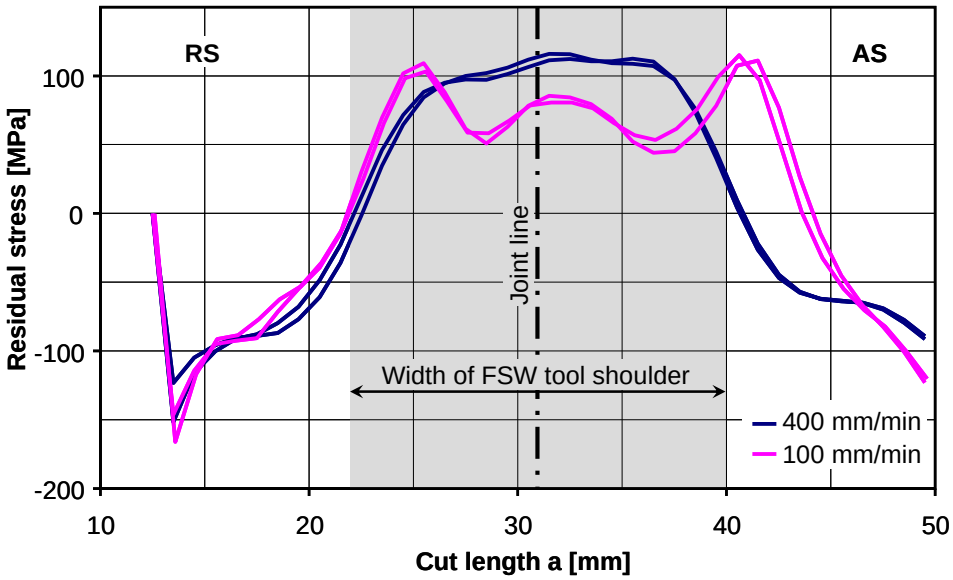

Figure 36 Distribution of longitudinal residual stresses in transverse CT specimens as calculated by the weight function method from the Krs distribution in Figure 35

As described in [3], residual stress intensity factors K_{rs} and the K_{eff}-approach can be used to clear crack growth data from residual stress effects. Thereby, the da/dN-ΔK_{eff} curves of the base material and the friction stir welds should fall in a common scatterband (if existent, remaining small differences have to be assigned to microstructural reasons). Conversely, K_{rs} data obtained for different welding conditions provide a basis to predict corresponding crack growth rates from base material behaviour. Based on a combination of cut-compliance measurements and the cutting technique described in [5, 6], it is furthermore planned to develop an engineering approach for the K_{rs} determination of cracks crossing T-joints.

[1] Schindler, H.-J., Cheng, W., Finnie, I. (1997) *Experimental Mechanics* 37, 272.
[2] Prime, M. B. (1999) *Fatigue and Fracture of Engineering Materials and Structures* 22, 195.
[3] Dalle Donne, C., Raimbeaux, G. (2001). In: *Proc. 10th Int. Conf. on Fracture ICF10*, pdf-file.
[4] Dalle Donne, C., Lima, E., Wegener, J., Pyzalla, A., Buslaps, T. (2001). In: *Proc. 3rd Int. Symp. on Friction Stir Welding*, pdf-file, TWI, UK.
[5] Galatolo, R., Lanciotti, A. (1997) *International Journal of Fatigue* 19, 43.
[6] Chiarelli, M., Lanciotti, A., Sacchi, M. (1999) *International Journal of Fatigue* 21, 1099.

5.4 Influence of Root Flaws on Fatigue Behaviour of Friction Stir Welded Joints

T. Vugrin (Airbus-D), J. Schneider and G. Biallas (DLR)

Friction stir welding (FSW) is a reliable process, and thus, welding flaws occur only sporadically. A flaw referred to as root flaw, may appear along the joint line near the lower surface of the welded sheets. It consists of micron-sized voids strung together and partially filled with (hydr)oxide particles as confirmed by numerous SEM and TEM investigations [1].

In certain cases the flaw line is proceeding to the nugget centre what would be designated as nugget flaw. There is strong evidence that surface (hydr)oxides are the origin of the root flaw, since the particles found in the voids have the same appearance as the surface layer formed on the aluminium sheets before welding. Hence, broken surface (hydr)oxide particles are mixed in

the weld nugget during the stirring process. This implies that root flaws are the more pronounced the thicker the former oxide scales on the sheets to be welded [1].

In the present study, the impact of root flaws on the fatigue behaviour of 2024 and 6013 FSW joints was investigated. Root flaws were created intentionally by a pre-oxidation treatment of the abutting sheet surfaces over 1 month at room atmosphere (RA) and over 5 minutes or 1 hour in vapour of boiling water respectively.

Due to the less intense material mixing applied during FSW of 6013, the remnants of the former (hydr)oxide surface layer could better be traced in the 6013 stirred zones as compared to those of 2024. Root flaws were originated in all FSW joints investigated, whereas nugget flaws could only be observed for 6013 5min/1h states. Specimens for S-N investigations were carefully polished to eliminate any notch effect, induced by the surface flash and ripples, but not to remove the root flaw bottom. The decrease in fatigue life caused by the root/nugget flaw was more apparent for 6013 samples as compared to 2024 material if the respective base material data were taken as a reference (Figure 37). For a less severe pre-oxidation, 2024 specimens still failed from primary particles in the heat affected zone resulting in fatigue lives nearly identical to those of the base material. Therefore, it can be concluded that a more intense material mixing associated with the smaller weld pitch as applied for 2024 is necessary, if natural oxidation of the sheets before welding has to be tolerated. Obviously, such intensified stirring promoted uniform distribution of the (hydr)oxide particles all over the weld nugget and restricted development of a solid root flaw line for FSW joints made from 2024 [2].

A fracture surface illustrating fatigue crack initiation from the root flaw region (indicated as RF in

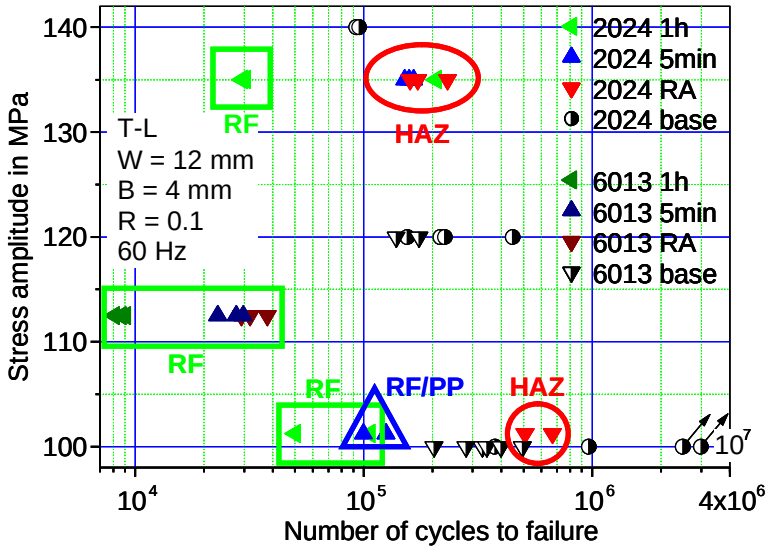

Figure 37 S-N fatigue curves, failure sites are indicated (RF: root flaw, HAZ: primary particles in the heat affected zone, RF/PP: both root flaw and primary particles in the flaw region)

Figure 37) is presented in Figure 38. In the lower line, the region highlighted by the green rectangle in the schematic was inspected more closely. This region displays the transition of the crack from the red root/nugget flaw line to the blue straight line, which is representing the area of stable fatigue crack growth. The root flaw region gave no evidence of any features suggesting cyclic crack growth. Contrarily, the dimple structure indicated a more monotonic type of failure. Thus, the root flaw probably opened within the first few cycles like a zipper, but at the same time the originating crack continuously inclined towards a direction more parallel to that of the acting load what reduced the effective stress intensity at the crack tip the more and more. At a

certain point, crack re-initiation was necessary to induce further crack growth in a direction perpendicular to the load as depicted by the blue straight line in Figure 38 [2]. The proposed crack re-initiation mechanism is also corroborated by the fact that loading at σ_a = 67.5 MPa (R = 0.1) consistently resulted in run-outs for all 2024 oxidation states, although crack initiation at root flaws was observed in some cases. This can be rationalised by a stress amplitude high enough to open the root flaw but too low to induce further crack growth in a direction perpendicular to the load.

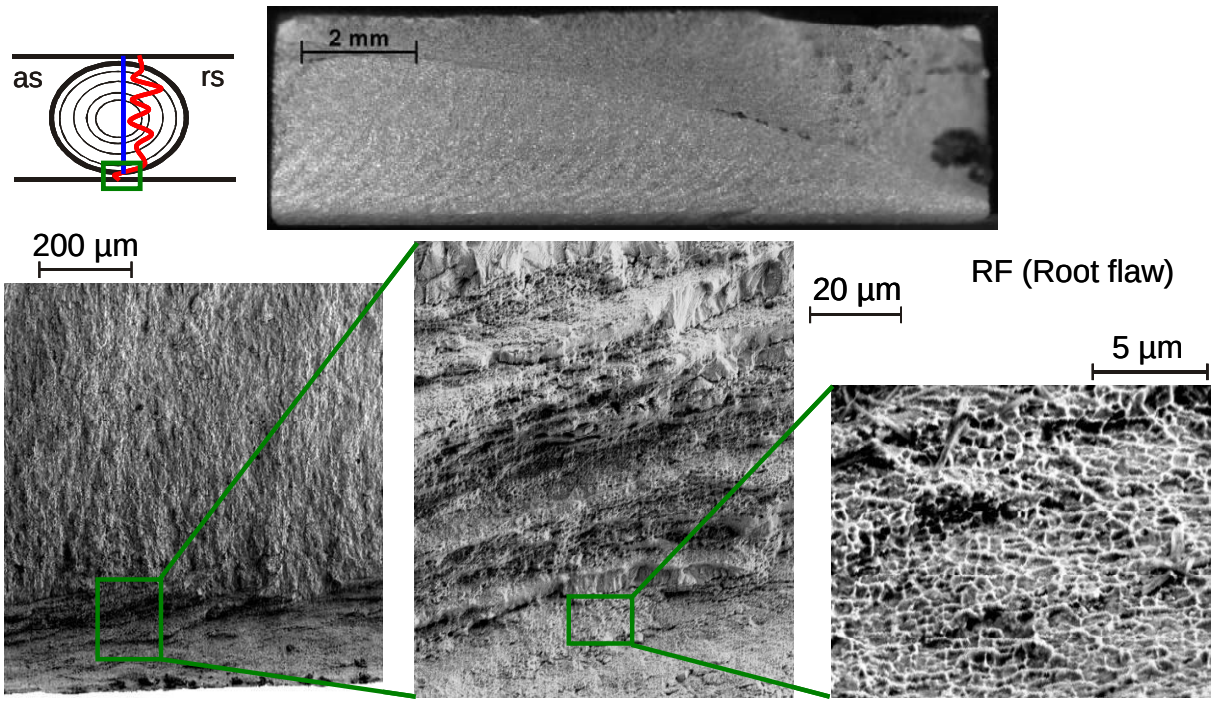

Figure 38 Fracture surface illustrating crack initiation from the root flaw region (6013 RA, σa = 112.5 MPa, Nf = 29900)

[1] Vugrin, T., Schmücker, M., Staniek, G. (2005). In: Proc. TMS Annual Meeting, San Francisco, 12.-16.02.2005, vol. III, pp. 277-284, Lienert, T. J. (Ed).
[2] Biallas, G., Vugrin, T., Schneider, J. (2007). In: Bruchmechanik und Bauteilsicherheit, Themenschwerpunkt Ermüdungsbruch - DVM-Bericht 239, pp. 83-92, DVM Berlin.

5.5 Experimental assessment of the crack deviation capabilities of FSW joints with pad-up

E. Hombergsmeier, V. Holzinger and C. Dalle Donne (EADS-IW)
Prof. A. Pirondi and D. Fersini (University Parma)

Friction Stir Welding (FSW) technology has been extensively investigated by Airbus in a number of applications for the wing and the pressurized fuselage. For fuselage applications, like the replacement of the riveted joints, a local reinforcing pad-up is used to give the weld area load-carrying capabilities comparable to the base material by means of a reduction of the local stress level.

A pad-up geometry, promoting crack deviation from the weld nugget (centre of the thick pad-up) to the thinner base material, would be considered preferable due to the current higher confi-

dence in predicting the crack propagation and residual strength behaviour of non-welded materials. Four different pad-up geometries (varying width and thickness) have been assessed according to their crack deviating capability, aiming to the definition of a suitable pad-up geometry for FSW fuselage panels. The tests have been performed with uniaxial loaded specimens as described in Figure 39. The investigation studied the damage tolerance response (crack propagation and residual strength) and crack path of the welded specimens in comparison to non-welded specimens having identical geometry.

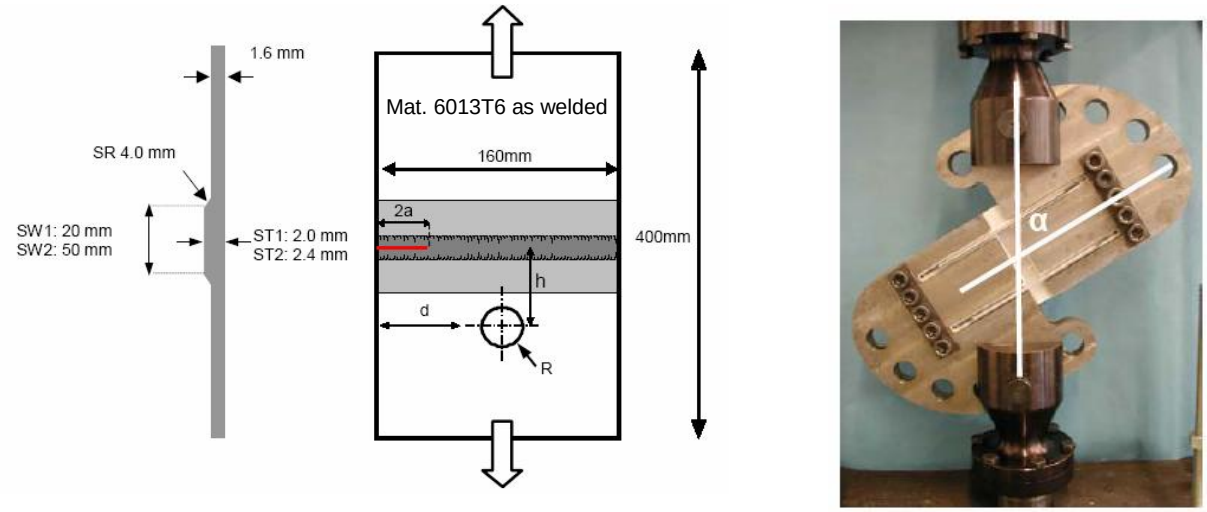

Figure 39 SE(T)-specimen with an offset hole. Important parameter is the distance h between the hole and specimen centreline [2]. The pad-up showing a crack path deviation at the greatest distance from the hole is considered superior. Testing was carried out under mode I loading and under mixed-mode loading, using a special clamping device giving a defined angle "α" (figure on the right). This angle enhance the crack path deviation during the experiments, if the mode I results are not satisfactory.

Finite element calculations with FRANC2D/L have been carried out, by Parma University, to establish meaningful specimens dimension and position of the hole. The maximum hoop stress criterion was used to predict the crack path. Due to the limited width of the specimens (160mm) the stress intensity factor was of the order of the fracture toughness of the material in the range of crack length of 40-50 mm. Under these circumstances, LEFM give only a first approximation of the experimental crack path. The comparison between simulation and the experiments shows a light underestimation of the crack path deviation even for base material.

During fatigue crack propagation tests, carried out under pure mode I load, all specimens experienced crack deviation. Large scatter made the interpretation of the effect of the pad-up difficult, significant distinctions between different pad-up geometries were not clearly identified. Several features like local microstructure, shape of the crack flanks, stress intensity and offset of the crack, influence the crack path.

Residual strength tests were carried out without offset hole under mode I and mixed-mode loading. They proved to be more appropriate for assessment of the role of the pad-up geometry in promoting crack deviation. Thick and narrow pad-up geometries gave higher tendency to crack deviation. The parent material was significantly more sensitive to crack deviation due to material homogeneity as shown in Figure 40.

In conclusion, within friction stir welds the crack has a higher tendency to stay within the weld Thermo Mechanical Effected Zone (TMAZ), even under significant Mode II loading. The soft TMAZ "channelled" the plastic deformation ahead of the crack tip, and hindered a path deviation of the plastic zone towards the pad-up edge as shown in Figure 40 (see also reference [1]).

To exploit the use of a local pad-up to promote crack deviation is rather a challenging task for homogeneous material and the complexity is significantly increased in case of a crack propagating is a soft weld nugget.

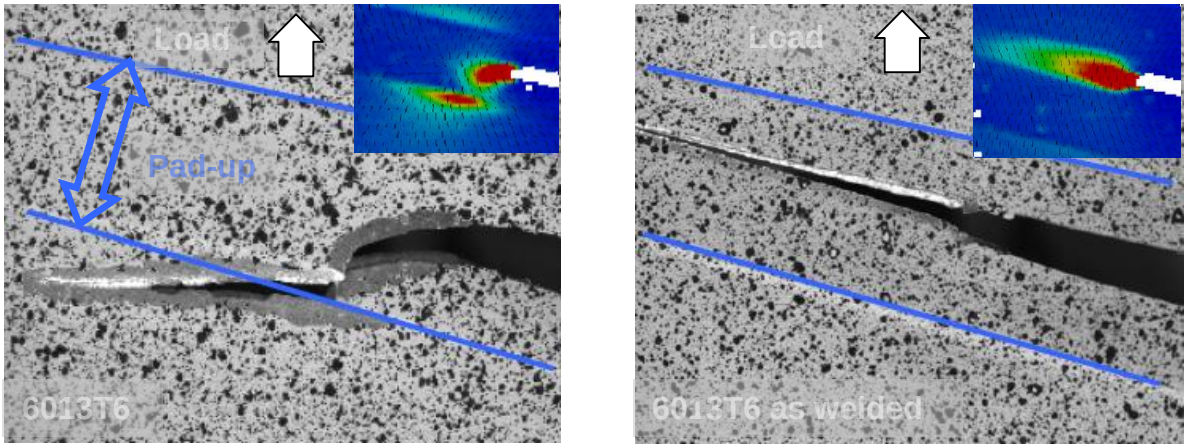

Figure 40 Examples of crack propagation during residual strength tests. Left: In the specimen without weld the crack deviates to the edge of the pad-up and then propagates along the pad-up edge in the low thickness area. Right: in comparable welded specimen the crack has higher tendency to propagate along the weld TMAZ, in the thick area of the specimen, without deviation

[1] Juricic, C., Dalle Donne, C. and Dreßler, U.: Effect of Heat Treatments on Mechanical Properties of Friction Stir Welded 6013, 3rd International Symposium on Friction Stir Welding, Kobe, Japan, 27 and 28 September 2001, TWI, 2001.

[2] Rubinstein, A.A.: Mechanics of crack path deviation, International Journal of Fracture 47, 1991, pp. 291-305.

5.6 Investigation of hybrid joint design based on FSW and bonding

E. Hombergsmeier and V. Holzinger (EADS-IW)

Friction Stir Welding (FSW) has been conventionally investigated in combination with integral design concepts with the main objective to reduce costs in comparison to the differential structure. The main designs considered are butt joints, overlap joints and T-joints aimed at replacing riveted or bonded joints.

A welded butt joint for primary aircraft structures generally requires a local pad-up of the weld area to compensate the detrimental effect of the welding process. For fuselage applications like the circumferential and longitudinal skin joints, the pad-up, with a thickness-increase ranging from 50% to 100%, is required to achieve damage tolerance, in particular large damage capability comparable with the base material. (The local pad-up creates a small weight penalty but significantly increases the necessary original material thickness, which is directly related to material costs.)

An innovative joint concept, based on the combination of FSW and structural metal bonding, replaces the local pad up with a bonded doubler on top of the weld, see Figure 41. The bonded part is a structural component and the resultant joint is intrinsically redundant for the case of failure or partial failure of one load path (weld nugget or bonded surface). This design principle has been developed in particular for fuselage and wing structures dominated by damage tolerance requirements.

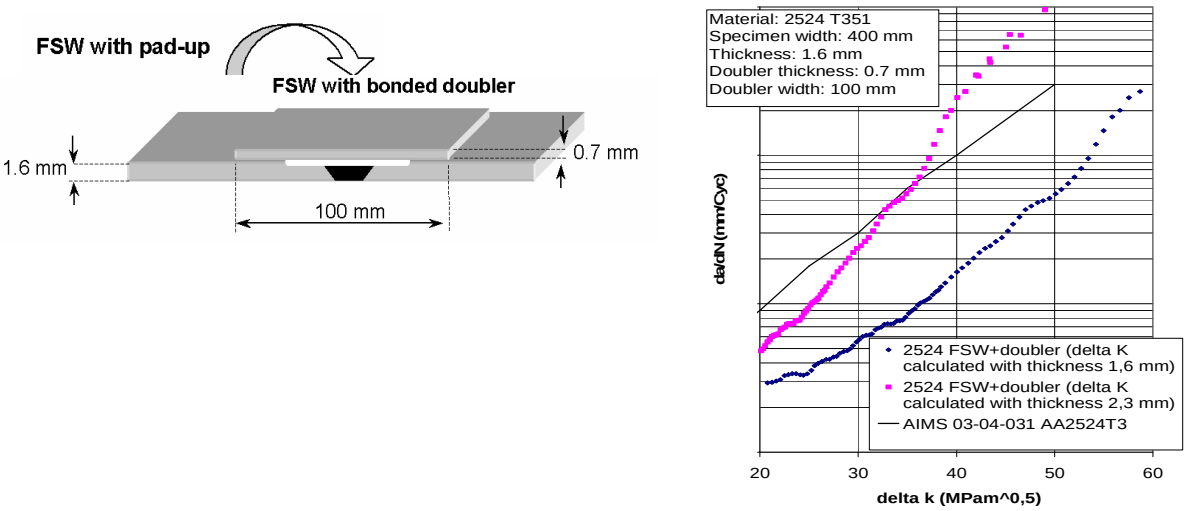

Figure 41 As alternative to the FSW-butt joint with pad up a FSW joint with doubler bonded on top of the weld. The crack propagation rate shows the high damage tolerance performances of such design principle

The mechanical performances have been investigated by Airbus and EADS Innovation Works in frame of the EU project DIALFAST. Coupons of 1.6 mm thick 2524T3 in as welded condition, with doublers of the same material having thickness of 0.7 mm, have been tested to determine static strength, fatigue life, crack propagation rate and residual strength (R-Curve).

Static properties are comparable to base material: the failure develops first by plastic deformation (necking) in parent material, then partial delamination of the bonded doubler occur to end with the fracture close to weld seam or in parent material. All fatigue failures take place at the run out of the bonded doubler: fatigue properties can be considered equivalent to parent material having a stress concentration similar to the one created by the doubler.

For the case of a through crack (in the weld and doubler) the crack propagation rate was one order of magnitude slower than 1.6mm non-welded material (see Figure 40). The calculation of ΔK according to a thickness equal to skin+doubler shows a faster crack propagation rate only for large ΔK (Figure 40). The R-Curve for the through crack was significantly higher than in the non-welded material having 1.6 mm thickness showing the potential benefit for areas of the structure where large damage capability is the main design driver.

Further investigations are currently on going to define the most appropriate local surface preparation of the weld in relation to the anticipated manufacturing concepts. Under screening is the corrosion response with standard bath application and local treatments inclusive of Cr_{VI} -free products.

[1] EU project 6th framework programme DIALFAST - Development of Innovative and Advanced Laminates for Future Aircraft Structures – Project No. 502846

6 Fatigue and Fracture of Metallic Fuselage Materials

6.1 Load sequence effects on fatigue crack growth in Al 2024-T351

D. Pöschmann, M. Schaper (TU Dresden)

Possible effects of loading interruptions, which are common when crack length measurements are done optically, as well as effects of overloads on fatigue crack growth in 1.6mm thick CCT specimens of Al2024-T351 were analysed. It was seen that intermittent unloading of up to several days had no measurable effect on subsequent crack growth rate. Both, single as well as multiple overloads of different magnitude and number caused the well-known retardation phenomenon.

In the initial stage the retardation proved to be highly similar with respect to time delay and retardation rate, but minimum growth rate and retarded growth increment were as expected related to both parameters. The striation spacings were observed to be significantly larger than the measured crack growth rate during both stationary loading and in the retardation region (the difference being larger at lower ΔK and growth rates). Obviously, several loading cycles are necessary for the formation of a single striation.

Additionally, at characteristic loading stages and plastic zone sizes, shear lips with changing orientation up to fully developed 45° inclined fatigue fracture surfaces were observed. These alterations in the mixed-mode growth behaviour were identified as the primary reasons behind the deviations in crack growth kinetics.

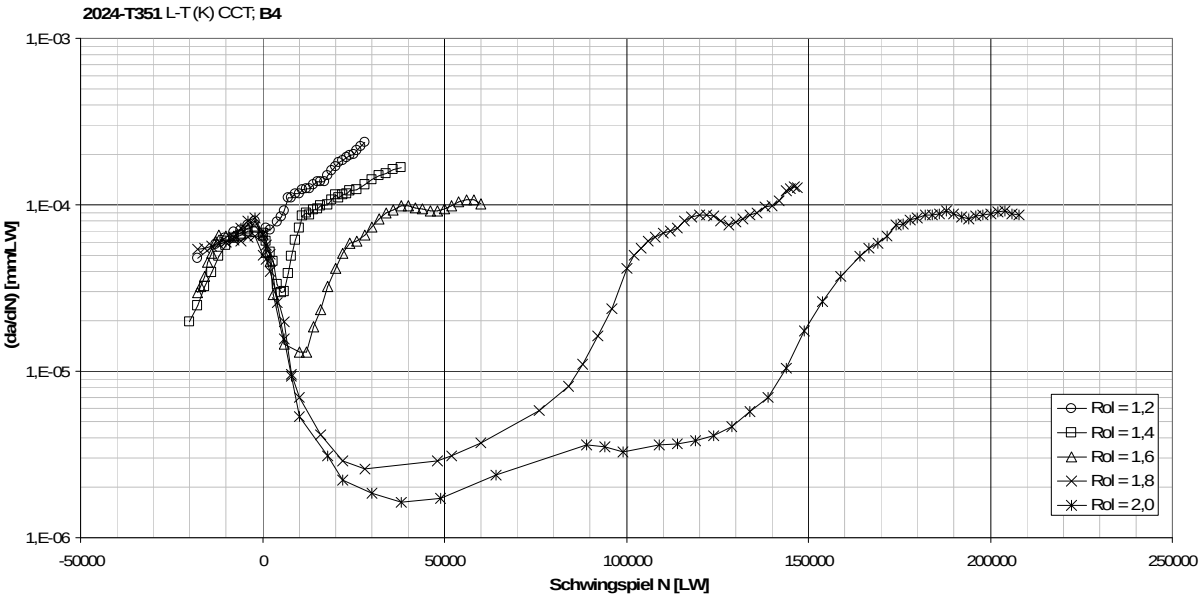

Figure 42 Crack growth retardation following overloads of indicated magnitudes

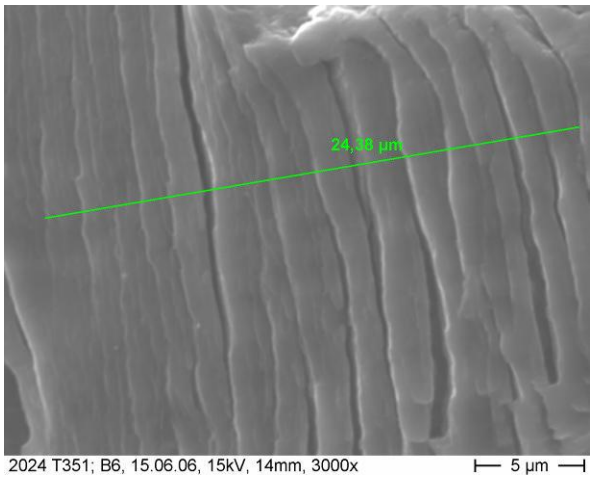

ΔK = 15 MPa*m$^{1/2}$

Δa $_{Str}$ = **1,5*10^{-3}mm**

da/dN = **4*10^{-4}mm/cycle**

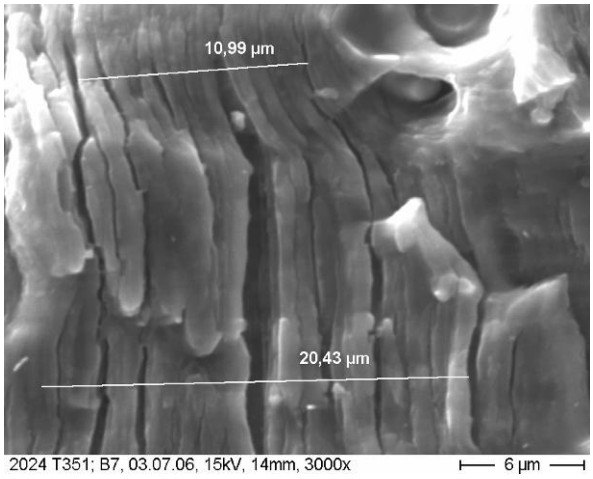

ΔK = 10 MPa*m$^{1/2}$

Δa $_{SwS}$ = **1*10^{-3}mm**

da/dN = **5*10^{-5}mm/cycle**

Figure 43 Striation spacing vs. measured crack growth rates at different ΔK levels

6.2 Influence of Load Sequences on Crack Propagation

R. Buchholz (IMA)

The load sequence has an important influence on the crack propagation behaviour. In order to determine this influence more precisely, crack propagation tests were performed with typical aviation load sequences. Therefore 2024-T351 and 7475-T7351 coupons, having either through-thickness cracks or edge cracks, were loaded after different load programs (i.e. constant amplitude, block program / marker loads and varying flight-by-flight schedules, Figure 44).

The tests were performed with an uniaxial servo-hydraulic test-rig; the nominal load values were generated and controlled separately by an external device. During the test, the crack length was measured optically by means of a travelling microscope. Subsequently, marker lines on the fractured surface were analysed by scanning electron microscopy.

The obtained results, together with further analysis, led to the development of a new crack propagation calculation method, taking the influence of former loads on the current crack propagation rate into account. The verification of this method is still in progress.

The two calculation methods (new versus conventional) are compared with respect to the experimental crack propagation values, as is shown in Figure 45. The new method closely follows the experimental values, whereas the conventional method drastically deviates from these values in an early stage.

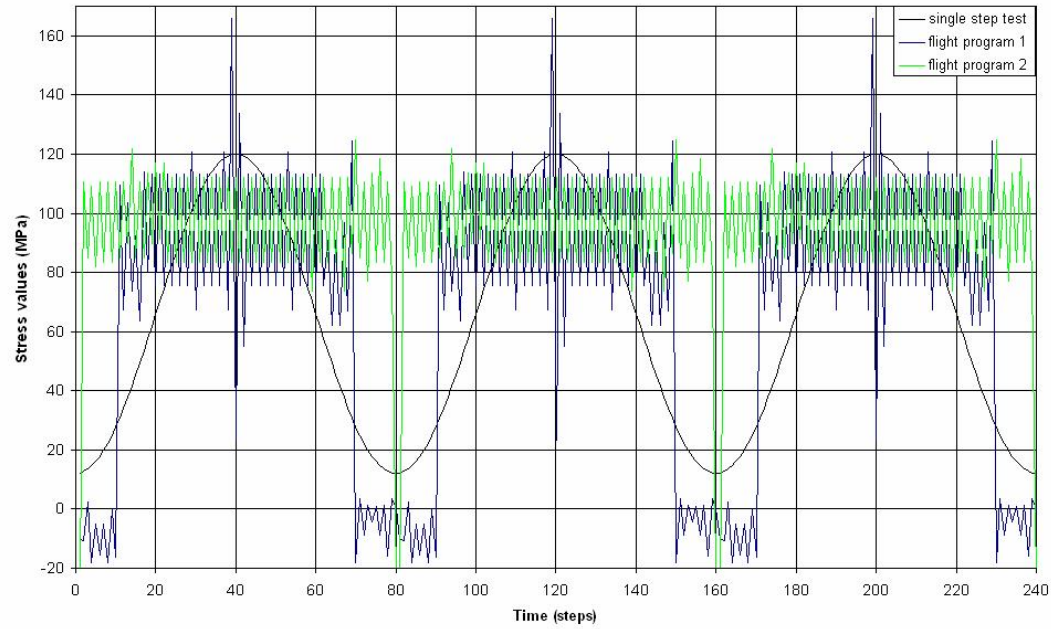

Figure 44 Examples of load spectra

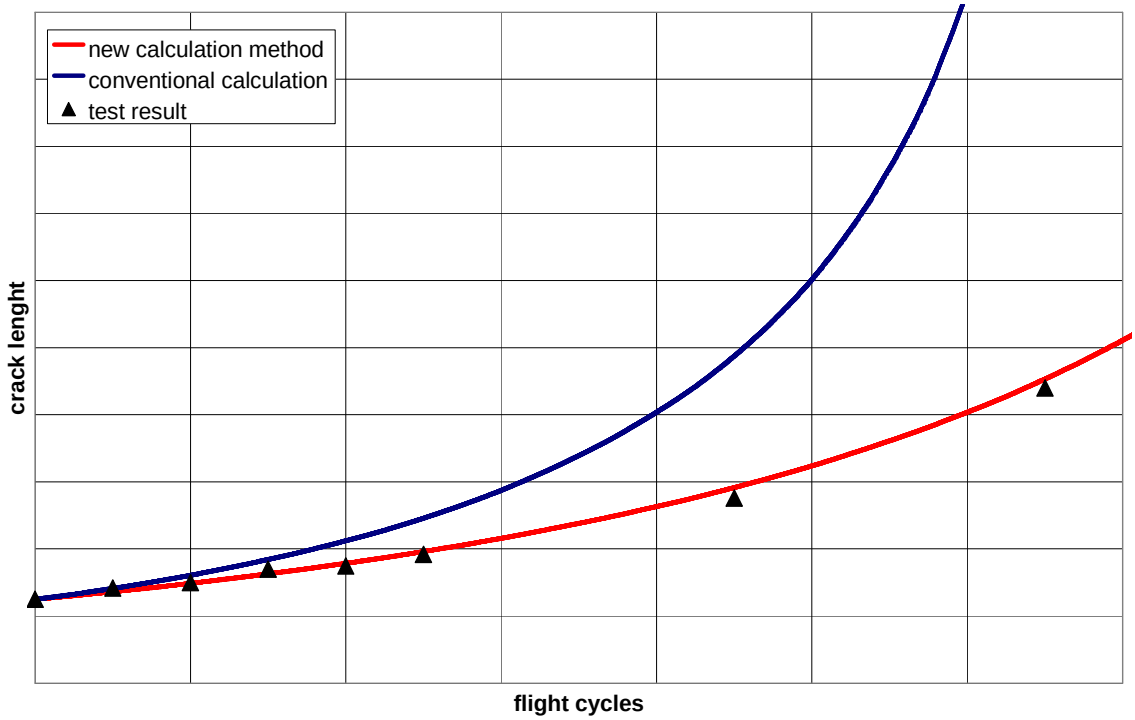

Figure 45 Crack grow curves (experimental and calculated results) for an edge cracked specimen (7475-T7351)

6.3 Modelling and analysis of crack turning on aeronautical structures

Llorenç Llopart (EADS-MAS)

Integral structures are a promising solution to meet actual aero-industry demands, offering weight reductions, cost savings and a higher corrosion resistance compared to riveted structures. But, in specific cases, its damage tolerance behaviour is lower than for differential structures. On the other hand, the holes on riveted structures are the major culprit in the development of multi-site damage fatigue, fretting corrosion, costly aircraft inspection, refurbishing and maintenance. Therefore, there is a large interest to find alternatives; integral and/or composites structures seem to be the most suitable candidates.

The damage tolerance behaviour and residual strength of integral structures have been identified to be improved by means of crack turning.

Of interest from the aeronautical industries' point of view, is to exploit the utilization of crack turning by means of a tailored design, in order to protect the stiffeners in front of an approaching skin-crack in integral structures. This resulted in a project at EADS Deutschland (Ottobrunn), with the aim to provide an existing modelling tool and a reliable criterion to asses and predict crack turning under nearly opening mode (Mode I) situations on structures, which represents aeronautical conditions. Because industries are mainly interested on quick and suitable design results, the feasibility to predict crack turning by means of Linear Elastic Fracture Mechanics (LEFM) and Finite Element Analysis (FEA) was studied.

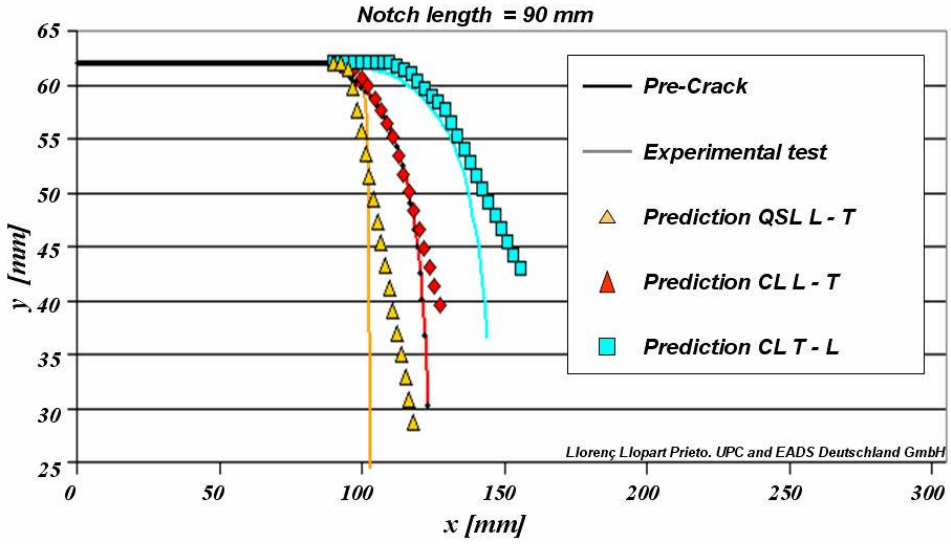

Figure 46 Crack path prediction for a 90 mm notched DCB specimen under quasi-static loading (QSL) and cyclic loading (CL) on T-L and L-T directions

Based on tests and simulations, a criterion was proposed, based on the work of Pettit [Crack turning in integrally stiffener Aircraft Structures. 2000] and the normalised T-stress, T_R, proposed by Pook [Crack Paths, WIT Press 2002].

The criterion takes the anisotropy of the material and the kind of loading into account, i.e. quasi-static or cyclic loading. Its reliability was successfully proved on Double Cantilever Beam (DCB) specimens (Figure 46) and a proof of confidence was furnished, clearing the way to apply crack turning for the design process on airplane structures loaded near Mode I.

6.4 Determination of the characteristic fatigue crack growth behaviour depending on K_{max} and R-ratio

J. Mladek and H.-J. Gudladt (UniBw-M)

Introduction

The lifetime of aircraft structures can be estimated by the summation of the time from crack initiation to the time of crack growth up to the final failure. Even when the time of fatigue crack growth represents the smaller part of the lifetime, the knowledge of the fatigue crack growth behaviour is essential to calculate the interval of inspection. It is generally known that fatigue crack propagation depends on the kind of material in use, the atmosphere (also known as environmental effects) and the loading conditions (especially at different mean stresses) [1]. Consequently, the present paper deals with the prediction of the fatigue crack growth behaviour of metallic materials for an expanded range of different loading conditions (R-ratios from -2 to 1) on the basis of experimental results. It will be shown that only some special crack propagation experiments are necessary to determine the crack growth rate (*da/dN*) as a function of the maximum stress intensity factor (K_{max}) and the stress ratio (R-ratio).

Experimental procedure

A usual way to determine the crack growth behaviour is to carry out threshold measurements as described in ASTM E 647 [2], also known as the load shedding method. During this experiment the load amplitude is reduced stepwise. Simultaneously, the R-ratio was kept constant (method A). This kind of experiment is performed on aluminium 6013 and the steels X5CrNi18-10 and C45E for different R-ratio; i.e. R = -2 (on 6013) / R = -1.5 (on steels), R = -1, R = 0.6 and R = 0.1.

In addition, another set of experiments has been done to measure the crack propagation behaviour. During these experiments, K_{max} was kept constant while K_{min} was increased. Consequently, the R-ratio increases and ΔK decreases until a threshold is reached (method B). To cover a wide range of loading conditions for the three materials this kind of experiment was carried out for three different K_{max} levels.

Results of the experiment plotted in 3D

In order to understand the influence of K_{max} and the R-ratio on the crack growth rate in more detail, the measured *da/dN* can be plotted versus K_{max} and R in a 3D presentation. Figure 47 shows the result of those experiments that were carried out on the steel X5CrNi18-10. Each curve shown in the figure results from one experimental run. Experiments according to method A are represented by curves with a constant R-ratio, while experiments after method B represent those curves, where the K_{max} level was kept constant. All curves taper to *da/dN* values lower than 10^{-11} m/cycles. That is when threshold ($K_{max,th}$) is reached.

For the prediction of the crack growth behaviour in a range of practical interest $K_{max,th} \leq K_{max} < K_{C,}$ one has to find a function for *da/dN* that depends on K_{max} and R. It should be possible to determine the parameters of this function *da/dN* = f (K_{max}, R) by using only a few crack propagation experiments.

Prediction model

To describe a single crack propagation curve for a constant R-ratio by a simple power law (equation 1) as it is given by Klesnil-Lukáš

$$da/dN = C \cdot \left(K_{\max}^{m} - K_{\max,th}^{m}\right) \qquad \text{Equation 1}$$

represents a good approximation to the experimental results [3]. In this function the *C* parameter describes the horizontal position of the curve which is dependant on the R-ratio, while parameter *m* represents the gradient of the *da/dN* curve, which is similar for different R values.

As it has been experimentally found, the threshold $K_{max,th}$ (*da/dN* ≈ 10^{-12} m/cycles) depends on the R-ratio, too. In order to expand the crack growth law, the influence of R has to be incorporated into equation 1. Consequently, *C*(R) and $K_{max,th}$(R) have to be taken into account. Now, equation 1 can be expressed as follows:

$$da/dN\left(K_{\max},R\right)=C(R)\cdot\left(K_{\max}^{m}-K_{\max,th}^{m}(R)\right). \qquad \text{Equation 2}$$

Now, in order to predict the crack propagation behaviour, one has to know *C*(R) and $K_{max,th}$ (R) in more detail.

At first, the characteristic of $K_{max,th}$(R) has been determined. Taking the relevant experiments into account, it was found that $K_{max,th}$(R) can be described by a hyperbolic function, as it is shown in equation 3.

$$K_{\max,th}(R)=K_{\max,th,crit}+\frac{\Delta K_{th,crit}}{(1-R)}. \qquad \text{Equation 3}$$

$K_{max,th,crit}$ and $\Delta K_{th,crit}$ can be found by adjusting the function on the experimentally determined thresholds $K_{max,th}$ plotted against the R-ratio. The quantities $K_{max,th,crit}$ and $\Delta K_{th,crit}$ represent the minimum loading condition (critical values) which have to be applied to cause crack growth. Figure 48 shows an excellent correlation between equation 3 and the experimental results for the three materials.

As a further step C(R) has to be developed. A method to get a function for C(R) is to use the crack propagation curve *da/dN*(R) after method B. Taking the given *da/dN*(R=-1) curve and the corresponding C(R=-1) value into account, C(R) can be calculated [4], as it is shown in equation 4.

$$C(R)=\frac{C(R=-1)\cdot\frac{da}{dN}(R)}{\frac{da}{dN}(R=-1)}. \qquad \text{Equation 4}$$

Figure 49 shows the predicted area for the crack growth behaviour as a function f (K_{max},R) for the steel X5CrNi18-10. A rather good correlation between the model prediction and the measured data has been found. Comparing the model calculations with the experimental results in a higher approximation, one can find regions where the model underestimates the reality. Consequently, the aim in near future will be to improve the presented model and to discuss the parameters of the function f(K_{max},R) in detail, taking made observation and the state of art knowledge on fatigue crack growth into account.

[1] Schwalbe K-H: Bruchmechanik metallischer Werkstoffe, 1 edn. Wien: Hanser; 1980.

[2] ASTM: Standard testing method for measurement of fatigue crack growth rates. In: *Annual Book of ASTM Standards.* Vol. 3.01. Philadelphia: ASTM; 1992: 647-701.

[3] Kohout J, Vechet S: A new function for fatigue curves characterization and its multiple merits. *International Journal of Fatigue* 2001, 23(2):175-183.

[4] Rödling S, Bär J, Gudladt H-J: Vorhersage des Ermüdungsrissausbreitungsverhaltens von Aluminiumlegierungen für Beanspruchungen mit variablen Mittelspannungen. *Materialwissenschaft und Werkstofftechnik* 2004, 35(6):401-406.

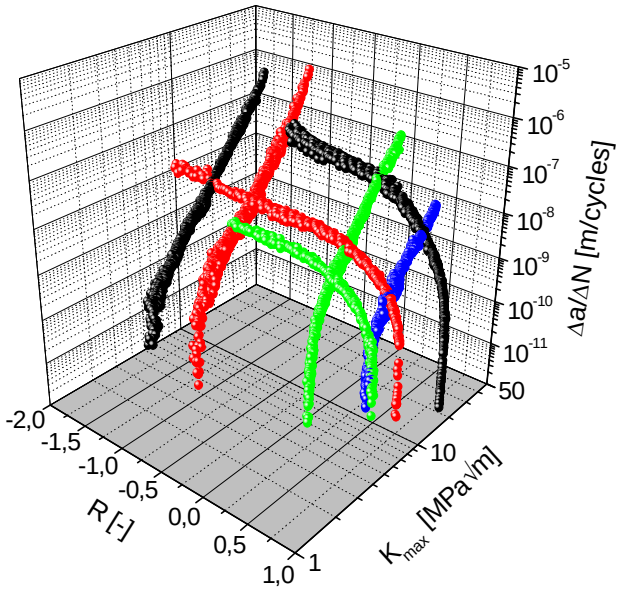

Figure 47 Crack propagation experiments on X5CrNi18-10 as *da/dN* vs. K_{max},R data

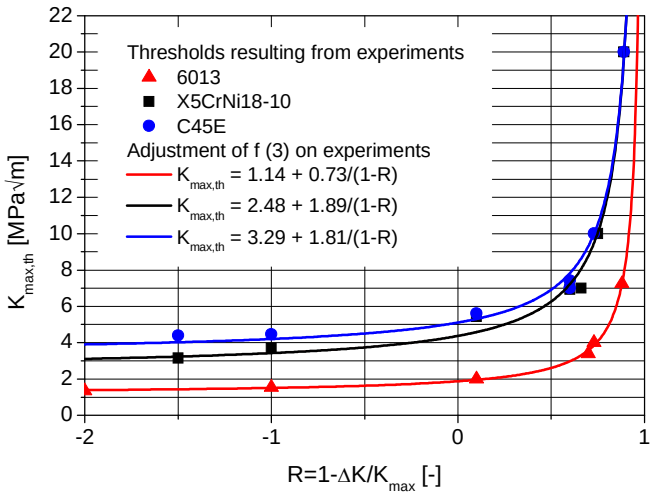

Figure 48 Experimentally acquired threshold and adjustment of equation 3 on experiments

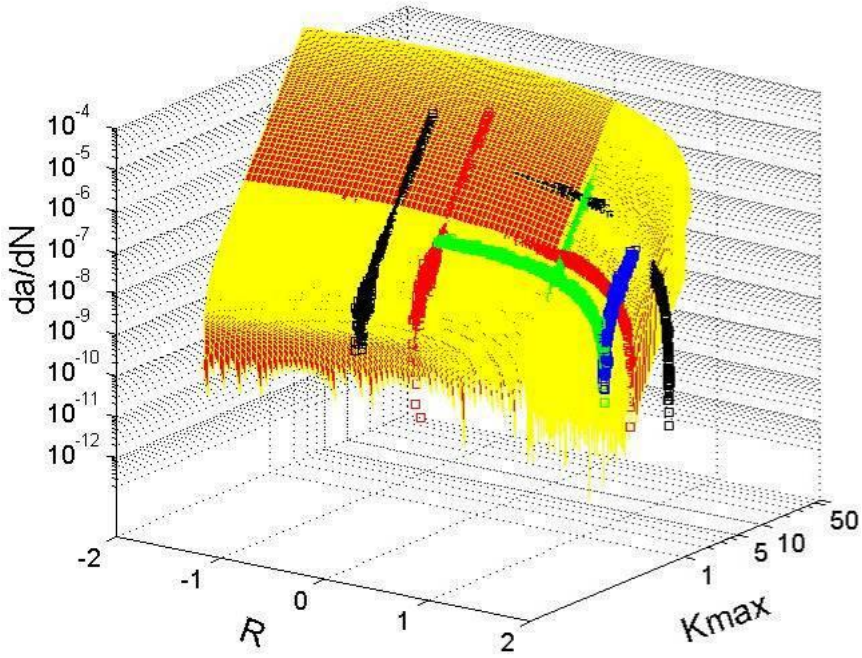

Figure 49 Predicted area of crack propagation in comparison with experiments on X5CrNi18-10

6.5 Regarding the Ratio of Tensile Strength to Shear Strength in General Strength Theory

L. G. Gelimson (RUAG)

To predict fatigue and fracture of metals [1], general strength theory [2] generalizes strength criteria and fits the substantial influence of the σ_u/τ_u ratio of the ultimate normal stress σ_u to the ultimate shear stress τ_u unlike common criteria with pre-defined values of this ratio. In combined bending and torsion with a normal stress σ and a shear stress τ at a point of a solid [biaxial stress state], the principal stresses σ_1, σ_2, σ_3 commonly ordered ($\sigma_1 >= \sigma_2 >= \sigma_3$) are

$$\sigma 1 = (\sigma + (\sigma^2 + 4\tau^2)^{1/2})/2,\ \sigma^2 = 0,\ \sigma^3 = (\sigma - (\sigma^2 + 4\tau^2)^{1/2})/2.$$

That pre-defined value is 2 and $3^{1/2}$ by the Tresca and Mises criteria [1], respectively,

$$\sigma_e = \sigma_1 - \sigma_3 <= \sigma_u\ ,\ \sigma_e = (\sigma_1^2 + \sigma_2^2 + \sigma_3^2 + \sigma_1\sigma_2 + \sigma_1\sigma_3 + \sigma_2\sigma_3)^{1/2} <= \sigma_u$$

[σ_e the equivalent uniaxial stress] giving in our case two particular and one unified criteria

$$\sigma_e = (\sigma^2 + 4\tau^2)^{1/2} <= \sigma_u\ ,\ \sigma_e = (\sigma^2 + 3\tau^2)^{1/2} <= \sigma_u\ ;\ \sigma_e = (\sigma^2 + (\sigma_u/\tau_u)^2\tau^2)^{1/2} <= \sigma_u\ .$$

To understand the naturalness of the last one, divide all its parts by σ_u:

$$(\sigma_e^\circ =)\ \sigma_e/\sigma_u = ((\sigma/\sigma_u)^2 + (\tau/\tau_u)^2)^{1/2} <= \sigma_u/\sigma_u\ (= 1)$$

with using relative (dimensionless) stresses (with the ° sign) introduced by the author [2].

For the general case of a triaxial stress state by using its three principal directions 1, 2, and 3 with vanishing all the shear stresses, first consider the Mises criterion. To take into account the unique additional constant σ_u/τ_u of a material, include one unknown factor *k*:

$$\sigma_e = (\sigma_1^2 + \sigma_2^2 + \sigma_3^2 + k(\sigma_1\sigma_2 + \sigma_1\sigma_3 + \sigma_2\sigma_3))^{1/2} <= \sigma_u$$

Note that uniaxial tension $\sigma_1 > 0$, $\sigma_2 = 0$, $\sigma_3 = 0$ gives that the factor at the sum $\sigma_1^2 + \sigma_2^2 + \sigma_3^2$ should be 1. To determine *k*, use combined bending and tension once more:

$$\sigma_e = (\sigma^2 + (2 - k)\,\tau^2))^{1/2} <= \sigma_u\ ,\ k = 2 - (\sigma_u/\tau_u)^2,$$
$$\sigma_e = (\sigma_1^2 + \sigma_2^2 + \sigma_3^2 + (2 - (\sigma_u/\tau_u)^2)\,(\sigma_1\sigma_2 + \sigma_1\sigma_3 + \sigma_2\sigma_3))^{1/2} <= \sigma_u\ .$$

For the Tresca criterion, it is impossible to keep the criterion's linear form by correction because its factors 1 and -1 are unique to provide its applicability to a uniaxial tension and compression $\sigma_1 = 0$, $\sigma_2 = 0$, $\sigma_3 < 0$, and introducing σ_2 brings nothing at least in the particular case of combined bending and torsion [σ_2 vanishes] and thus cannot solve, all the more, the general problem. Now it is natural to choose a similar quadratic form of a formula

$$\sigma_e = ((\sigma_1 - \sigma_3)^2 + k\sigma_1\sigma_3)^{1/2} <= \sigma_u\ .$$

The same combined bending and torsion leads to

$$\sigma_e = (\sigma^2 + (4 - k)\,\tau^2))^{1/2} <= \sigma_u\ ,\ k = 4 - (\sigma_u/\tau_u)^2,$$
$$\sigma_e = ((\sigma_1 - \sigma_3)^2 + (4 - (\sigma_u/\tau_u)^2)\,\sigma_1\sigma_3)^{1/2} <= \sigma_u\ ,\ \sigma_e = (\sigma_1^2 + \sigma_3^2 + (2 - (\sigma_u/\tau_u)^2)\,\sigma_1\sigma_3)^{1/2} <= \sigma_u\ .$$

Experimental data on strength of ductile materials is often placed between the curves given by the Tresca and Mises criteria. Expecting more criterion precision by smaller deviation of the σ_u/τ_u ratio from its pre-defined value gives the unified criterion as the linear combination

$$\sigma_e = ((\sigma_u/\tau_u)^2 - 3)\,(\sigma_1 - \sigma_3) + (4 - (\sigma_u/\tau_u)^2)\,(\sigma_1^2 + \sigma_2^2 + \sigma_3^2 + \sigma_1\sigma_2 + \sigma_1\sigma_3 + \sigma_2\sigma_3)^{1/2} <= \sigma_u\ .$$

The unified criterion using the criteria forms already corrected by the present methods is

$$\sigma_e = ((\sigma_u/\tau_u)^2 - 3)\,(\sigma_1^2 + \sigma_3^2 + (2 - (\sigma_u/\tau_u)^2)\,\sigma_1\sigma_3))^{1/2} +$$
$$(4 - (\sigma_u/\tau_u)^2)\,(\sigma_1^2 + \sigma_2^2 + \sigma_3^2 + (2 - (\sigma_u/\tau_u)^2)\,(\sigma_1\sigma_2 + \sigma_1\sigma_3 + \sigma_2\sigma_3))^{1/2} <= \sigma_u\ .$$

Note that such a linear unification approach is not the only. To naturally extend it, a power unification approach can be also used. And the Hosford exponential unification [3]

$$\sigma_e = (((\sigma_1 - \sigma_2)^k + (\sigma_2 - \sigma_3)^k + (\sigma_1 - \sigma_3)^k)/2)^{1/k} <= \sigma_u$$

of the Tresca and Mises criteria gives them by $k = 1$ and $k = 2$. To provide these values of *k* using the same pre-defined values of the σ_u/τ_u ratio for the both criteria, naturally choose $k = 5$ -

$(\sigma_u/\tau_u)^2$. For further generalizations, introduce the notation (with apparently extending for any sets of variables and function values)

$f(x, y \mid f(a, b) = v, f(c, d) = w)$

for any function taking, e.g., values v and w by values a, b and c, d of its variables x, y, respectively. Then choose instead of $(\sigma_u/\tau_u)^2$ - 3, 4 - $(\sigma_u/\tau_u)^2$ and $k = 5 - (\sigma_u/\tau_u)^2$, respectively:

$f(\sigma_u/\tau_u \mid f(2) = 1, f(3^{½}) = 0)$,

$g(\sigma_u/\tau_u \mid g(2) = 0, g(3^{½}) = 1)$,

$h(\sigma_u/\tau_u \mid h(2) = 1, h(3^{½}) = 2)$.

[1] Handbuch Struktur-Berechnung. Prof. Dr.-Ing. L. Schwarmann. Industrie-Ausschuss-Struktur-Berechnungsunterlagen, Bremen, 1998

[2] Gelimson, L. G.: General Strength Theory. Abhandlungen der Wissenschaftlichen Gesellschaft zu Berlin, Publisher Prof. Dr. habil. V. Mairanowski, 3 (2003), Berlin, 56–62

[3] Hosford, W. F. A generalized isotropic yield criterion. Trans. A. S. M. E., Ser. E 2 (1972), 290-292

7 Fatigue and Fracture of Composites

7.1 Correcting and Further Generalizing Critical State Criteria in General Strength Theory

L. G. Gelimson (RUAG)

For predicting fatigue and fracture of composites [1], general strength theory [2] generalizes strength criteria and fits the substantial influence [3] of the intermediate normal stress via introducing additional material constants. Suppose in limiting states, the equivalent stress σ_e be no constant limiting stress σ_l (in tension σ_t and in compression σ_c) but a linear function of the ordered principal stresses $\sigma_1 \geq \sigma_2 \geq \sigma_3$ via equation

$$\lambda_0 F(\sigma_1, \sigma_2, \sigma_3) + \lambda_1\sigma_1 + \lambda_2\sigma_2 + \lambda_3\sigma_3 = \lambda_4 \; [\lambda_0, \lambda_1, \lambda_2, \lambda_3, \lambda_4 \text{ constants}]$$

where F is the function in general limiting criterion $\sigma_e = F(\sigma_1, \sigma_2, \sigma_3) = \sigma_l$. For the Tresca criterion with $F(\sigma_1, \sigma_2, \sigma_3) = \sigma_1 - \sigma_3$, using data on uniaxial tension and compression gives the criterion with an additional constant x of the material:

$$\sigma_e = \sigma_1 + x\sigma_2 - \sigma_3 = \sigma_l.$$

The physical sense of this constant x is that it is the uniaxial limiting stress σ_l divided by the limiting stress in hydrostatic tension σ_{ttt}. The last can be hardly determined directly but can be obtained by using the data on a third experiment with $\sigma_2 \neq 0$, hence pure shear is not suitable. In biaxial compression, $\sigma_1 = 0$, $\sigma_2 = \sigma_3 = -\sigma_{cc}$ we have $x = 1 - \sigma_l/\sigma_{cc}$, in triaxial tension and compression $\sigma_1 = \sigma_{tcc}$, $\sigma_2 = \sigma_3 = -\sigma_{tcc}$ the result is $x = 2 - \sigma_l/\sigma_{tcc}$.

Analogously correcting the Mises criterion and that general limiting criterion gives criteria

$$\sigma_e = \sigma_i = \{[(\sigma_1 - \sigma_2)^2 + (\sigma_2 - \sigma_3)^2 + (\sigma_3 - \sigma_1)^2]/2\}^{1/2} + x\sigma_2 = \sigma_l,$$

$$\sigma_e = F(\sigma_1, \sigma_2, \sigma_3) + x\sigma_2 = \sigma_l.$$

Further generalizing method to extend strength laws hierarchies [2] gives equations

$$G(\sigma_1^0, \sigma_2^0, \sigma_3^0) = \lambda_0 + \lambda_1\sigma_1^0 + \lambda_2\sigma_2^0 + \lambda_3\sigma_3^0, \; G(\sigma_1^0, \sigma_2^0, \sigma_3^0) = H(\sigma_1^0, \sigma_2^0, \sigma_3^0)$$

where G, H are certain (maybe unknown unlike F) different functions of the reduced (relative) principal normal stresses σ_1^0 , σ_2^0 , σ_3^0 and possibly of some pure constants of a material. For example, using the data on uniaxial tension and compression gives the structure

$$\sigma_e = F(\sigma_1, \sigma_2, \sigma_3)/(1 + \lambda) + \lambda(\sigma_1 - \sigma_3)/(1 + \lambda) + x\sigma_2 = \sigma_l$$

having two additional constants λ and x of a material. The experimental data on hypothetical uniform triaxial tension $\sigma_1 = \sigma_2 = \sigma_3 = \sigma_{ttt}$ and torsion $\sigma_1 = \tau_l$, $\sigma_2 = 0$, $\sigma_3 = -\tau_l$ gives criterion

$$\sigma_e = (2\tau_l - \sigma_l)F(\sigma_1, \sigma_2, \sigma_3)/[2\tau_l - F(\tau_l, 0, -\tau_l)] +$$
$$[\sigma_l - F(\tau_l, 0, -\tau_l)](\sigma_1 - \sigma_3)/[2\tau_l - F(\tau_l, 0, -\tau_l)] + \sigma_l\sigma_2/\sigma_{ttt} = \sigma_l.$$

Let the potential energy of deformation, multiplied by the maximum shear stress, be a certain linear combination of the principal stresses. Using uniaxial tension, uniaxial and uniform biaxial compression $\sigma_1 = 0$, $\sigma_2 = \sigma_3 = -\sigma_{cc}$ to the criterion in the reduced principal stresses

$$(\sigma_1^0)^2 + (\sigma_2^0)^2 + (\sigma_3^0)^2 - 2\mu[(\sigma_1^0)^2(\sigma_2^0)^2 + (\sigma_2^0)^2(\sigma_3^0)^2 + (\sigma_1^0)^2(\sigma_3^0)^2] =$$
$$1 + [1 - 2(1 - \mu)(\sigma_{cc}^0)^2](\sigma_2^0)^2/(\sigma_1^0 - \sigma_3^0)$$ [μ the Poisson ratio, $\sigma_{cc}^0 = \sigma_{cc}/\sigma_c$].

For the squared maximum shear stress and the maximum shear stress multiplied by the octahedral shear stress, respectively, we obtain criteria

$$\sigma_1^0 - \sigma_3^0 = 1 + (1 - \sigma_{cc}^0)\sigma_2^0/(\sigma_1^0 - \sigma_3^0),$$
$$\sigma_i^0 = 1 + (1 - \sigma_{cc}^0)\sigma_2^0/(\sigma_1^0 - \sigma_3^0).$$

By designation $\sigma_{cc}^0 = \sigma_{cc}/\sigma_c$ (the reduced limiting stress in uniform biaxial tension), these two criteria give $\sigma_{tt}^0 + \sigma_{cc}^0 = 2$ and can be adequate only under this condition. The analogous assumption for the maximum shear stress multiplied by the squared octahedral shear stress leads to the criterion [with its necessary condition $(\sigma_{tt}^0)^2 + (\sigma_{cc}^0)^2 = 2$]:

$$(\sigma_i^0)^2 = 1 + [1 - (\sigma_{cc}^0)^2]\sigma_2^0/(\sigma_1^0 - \sigma_3^0).$$

Let the squared maximum shear stress in critical states of an isotropic material with equal strength in tension and compression be equal to a certain linear combination of the limiting uniaxial stress and the principal stresses. Four experimental data on uniaxial and uniform biaxial tensions and compressions then give the criterion

$$(\sigma_{tt}^0 + \sigma_{cc}^0)(1 - \sigma_{tt}^0\sigma_{cc}^0)(\sigma_1^0 - \sigma_3^0) + (2\sigma_{tt}^0\sigma_{cc}^0 - \sigma_{tt}^0 - \sigma_{cc}^0)(\sigma_1^0 - \sigma_3^0)^2 +$$
$$(\sigma_{cc}^0 - \sigma_{tt}^0)(1 - \sigma_{tt}^0)(1 - \sigma_{cc}^0)\sigma_2^0 = \sigma_{tt}^0\sigma_{cc}^0(2 - \sigma_{tt}^0 - \sigma_{cc}^0).$$

The analogous hypothesis as applied to the squared octahedral shear stress or the potential energy of distortion by the same experimental data leads to the criterion

$$(\sigma_{tt}^0 + \sigma_{cc}^0)(1 - \sigma_{tt}^0\sigma_{cc}^0)(\sigma_1^0 - \sigma_3^0) + (2\sigma_{tt}^0\sigma_{cc}^0 - \sigma_{tt}^0 - \sigma_{cc}^0)(\sigma_i^0)^2 +$$
$$(\sigma_{cc}^0 - \sigma_{tt}^0)(1 - \sigma_{tt}^0)(1 - \sigma_{cc}^0)\sigma_2^0 = \sigma_{tt}^0\sigma_{cc}^0(2 - \sigma_{tt}^0 - \sigma_{cc}^0).$$

[1] Handbuch Struktur-Berechnung. Prof. Dr.-Ing. L. Schwarmann. Industrie-Ausschuss-Struktur-Berechnungsunterlagen, Bremen, 1998

[2] Gelimson, L. G.: General Strength Theory. Abhandl. der Wissenschaftlichen Gesellschaft zu Berlin, Publisher Prof. Dr. habil. V. Mairanowski, 3 (2003), Berlin, 56–62

[3] P. W. Bridgman, Collected Experimental Papers, Vols. 1 to 7, Harvard University Press Publ., Cambridge (Massachusetts), 1964

7.2 Corrections and Generalizations of the Absolute and Relative Errors

L. G. Gelimson (RUAG)

By estimating any inexact data, for the simplest formal (correct or not) equality $a =? b$ with two real numbers, the absolute error $|a - b|$ [1] alone offers no sufficient quality estimation giving, e.g., the same result 1 for the acceptable formal equality 1000 =? 999 and for the inadmissible one 1 =? 0.

This error is not invariant by equivalent transformations of a problem because, for instance, when multiplying a formal equality by a nonzero number, the absolute error is multiplied by the modulus (absolute value) of that number. For the relative error [1], there are at once two propositions, namely to use either $|a - b|/|a|$ or $|a - b|/|b|$ as an estimating fraction, which is a generally inadmissible uncertainty that could be acceptable only if $|a/b|$ is close to 1.

Further the relative error should always belong to the segment [0, 1]. But for 1 =? 0 by choosing 0 as the denominator, the result is $+\infty$, for 1 =? -1 by each denominator choice the result is 2. Hence, the relative error has a restricted range of applicability. By more complicated formal equalities with at least three elements, e.g., by 100 - 99 =? 0 or 1 - 2 + 3 - 4 =? -1, the choice of a denominator seems to be vague at all.

For a general problem setting, let $Z \subseteq X \times Y$ be any given subset of the direct product of two sets X and Y and have a projection Z/X on X consisting of all $x \in X$ really represented in Z, i.e., of all such x that for each of them there is a $y \in Y$ such that $(x, y) \in Z$. Let further $\{ y = F(x) \}$ ($x \in X$, $y \in Y$) be a certain class of functions defined on X with range in Y. Then the graph of such a function is a curve in $X \times Y$.

The problem consists in finding (in this class) functions with graphs nearest to Z in a certain reasonable sense. To exactly fit this with a specific function $y = F(x)$, the set Z has to be included in the graph of this function: $Z \subseteq \{ (x, F(x)) \mid x \in X \}$, or, equivalently, $F(x) = y$ for each $x \in Z/X$. But this inclusion (or equality) does not necessarily hold in the general case. Then it seems to be reasonable to estimate the error $E(F(x) =? y \mid x \in Z/X)$ of the formal equality (true or not true) $F(x) =? y$ on this set Z/X via a certain error function E defined at least on Z/X.

To suitably construct such a function, it seems to be reasonable to first consider two stages of its building:

1) defining *local* error functions to estimate errors at separate points x;
2) defining *global* error functions using the values of local error functions to estimate errors on the whole set Z/X. Possibly the simplest and most straightforward approach includes the following steps:

- defining on $Y \times Y$ certain nonnegative functions $r_{yy'}(y, y')$ generally individual for different y, y' and, e.g., similar to a distance [1] between any two elements y, y' of Y (but not necessarily with holding the distance axioms [1]),
- defining certain nonnegative functions $R_x(r(F(x), y))$ generally individual for different x, summing (possibly including integrating) their values on Z/X, and
- using this sum (possibly including integrals) as a nearness measure.

Elastic mathematics [2] proposes an auto-error irreproachably correcting the relative error and generalizing it possibly for any conceivable range of applicability. For $a =? b$, the linear estimating fraction is $\delta_{a =? b} = |a - b|/(|a| + |b|)$ by $|a| + |b| > 0$, which should simply vanish by $a = b = 0$. Introduce *extended division:* $a//b = a/b$ by $a \neq 0$ and $a//b = 0$ by $a = 0$ independently of the existence and value of b. Then $\delta_{a =? b} = |a - b|//(|a| + |b|)$. The quadratic estimating fraction is ${}^2\delta_{a =? b} = |a - b|//[2(a^2 + b^2)]^{1/2}$. The outputs (return values) of such auto-errors always belong to [0, 1]. By the principle of tolerable simplicity [2], it is reasonable to use the linear estimating fraction alone if it suffices. For a formal vector equality $\sum_{\omega\in\Omega} z_\omega =? 0$,

$$\delta(\textstyle\sum_{\omega\in\Omega} z_\omega =? 0) = ||\sum_{\omega\in\Omega} z_\omega||//\sum_{\omega\in\Omega}||z_\omega||,\ {}^2\delta(\sum_{\omega\in\Omega} z_\omega =? 0) = ||\sum_{\omega\in\Omega} z_\omega||//((Q(\Omega)\sum_{\omega\in\Omega}||z_\omega||^2)^{½}$$

whose denominators contain all elements that have been initially in the equality, i.e., before any transformations. If all the vectors are replaced with numbers, the norms can be replaced with the moduli (absolute values). Examples:

$$\delta_{100 - 99 =? 0} = 1/199 = \delta_{100 =? 99};\ \delta_{1 - 2 + 3 - 4 =? -1} = |1 - 2 + 3 - 4 + 1|/(1 + 2 + 3 + 4 + 1) = 1/11.$$

The absolute error, the relative error, and the auto-error of any *exact* object or model always vanish. It is often reasonable to additionally discriminate exact objects or models by the *confidence* in their *exactness reliability*.

For example, both $x_1 = 1 + 10^{-10}$ and $x_2 = 1 + 10^{10}$ are exact solutions to the inequation $x > 1$, x_1 practically unreliable and x_2 guaranteed. Their discrimination is especially important by any inexact data. Traditional mathematics [1] cannot provide this at all. Elastic mathematics [2] proposes for this purpose the basic concept of the reserve which is quite new in mathematics and extends the auto-error in the following sense.

The values of an auto-error H belong to the segment [0, 1], those of a reserve R to [-1, 1]. For each *inexact* object I, $H(I) > 0$ and we can take $R(I) = -H(I)$. For each *exact* object E, $H(E) = 0$ and $R(E) \geq 0$. A proposition to determine the reserve of an *inexact* object as its auto-error with the opposite sign is at once evident.

For an *exact* object, it seems to be reasonable, to first define a suitable mapping of the object with respect to its exactness boundary and to further take the auto-error of the mapped object. It is exact if and only if the object itself precisely lies on its exactness boundary where the reserve vanishes. Otherwise, the mapped object is inexact and the object itself has a positive reserve. For inequalities, such a mapping can be replaced with negating inequality relations and conserving equality ones. In our example, we have

$$R_{x>1}(x_1) = R_{x>1}(1 + 10^{-10}) = H_{x<?1}(1 + 10^{-10}) = 10^{-10}/(2 + 10^{-10}),$$
$$R_{x>1}(x_2) = R_{x>1}(1 + 10^{10}) = H_{x<?1}(1 + 10^{10}) = 10^{10}/(2 + 10^{10}).$$

[1] Encyclopaedia of Mathematics. Ed. M. Hazewinkel. Volumes 1 to 10. Kluwer Academic Publ., Dordrecht, 1988-1994

[2] Gelimson, L. G.: Elastic Mathematics. General Strength Theory. The ”Collegium” International Academy of Sciences Publishers, Munich, 2004

8 Fatigue and Fracture of Engine Materials and Structures

8.1 Low Cycle and Thermo-mechanical Fatigue Behaviour of Designated HP Compressor Materials based on Ti-Al

T.K. Heckel and H.-J. Christ (Uni Siegen)

As energy conversion systems require higher efficiencies in the future, γ-TiAl-based intermetallics became a promising candidate for substituting nickel-base or titanium alloys, especially with respect to specific stiffness which surpasses 40 GPa*cm^3/g in γ-TiAl and is some 27 GPa*cm^3/g in both, Ni and Ti alloys. The necessity for lighter and stiffer materials is especially obvious in the high-pressure compressor of jet engines. High-temperature Ti alloys like Ti6242, IMI834 or Ti1100 offer a long-term maximum operating temperature around 500°C. However, as the compressor outlet temperature is about 650°C, heavy nickel-base alloys have to be used in the last stages. The temperature limitations in Ti alloys arise primarily from poor oxidation behaviour and the potential risk of Ti fire. Advanced γ-TiAl alloys may be capable of replacing Ni-base alloys, leading to substantial weight savings of up to 100 kg in a single jet engine if γ-TiAl is introduced.

The increase in strength, ductility and oxidation resistance of 3rd generation γ-TiAl, to which the investigated alloy TNB-V2 belongs, is caused by a relatively high content of niobium (5-10 at%). TNB alloys may fill the temperature-gap where near-α Ti alloys like Ti6242 loose their superiority, and where Ni-base alloys (e.g. IN718) are unfavourable because of their high density.

Isothermal and thermo-mechanical fatigue of Ti6242 and TNB-V2 was investigated. Ti6242, a near-α alloy, was used as a reference material as it is exposed to similar service conditions as supposed for TNB-V2. Fully reversed isothermal tests were conducted at a strain amplitude of 0.7%. The temperature ranged from 350 to 650°C in case of Ti6242 and from 550 to 850°C for TNB-V2, enabling a comparison of the materials behaviour between 550 and 650°C. At 550°C, TNB-V2 reached 20% of the lifetime of Ti6242, while at 650°C it reached 45%, Figure 50.

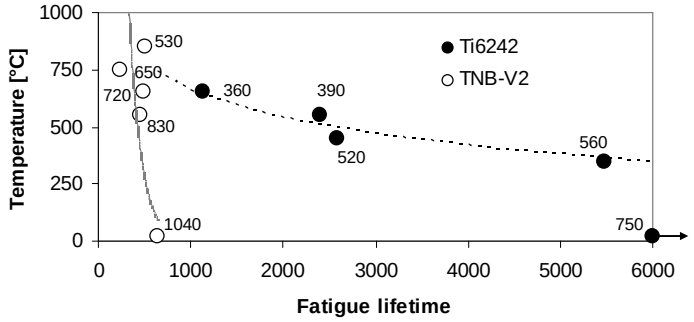

Figure 50 Temperature versus lifetime for Ti6242 and TNB-V2 under identical testing conditions ($\Delta\varepsilon_t/2$ = 0.7%), room temperature test of Ti6242 was stopped after 40,000 cycles. Stress amplitudes in MPa at half life are indicated for each test

Thermo-mechanical tests were conducted to investigate the possibility to predict this behaviour from isothermal data. For Ti6242, the results revealed that under in-phase loading the material exhibits a performance similar to isothermal conditions at the maximum temperature, Figure 51. Neither for Ti6242 under out-of-phase load (Figure 51), nor for TNB-V2 under any TMF condition (Figure 52), a similarity to isothermal tests was found. For both alloys, fatigue lifetime under

out-of-phase loading was shorter as compared to in-phase conditions, leading to the assumption that environmental damage is most pronounced. Tests in vacuum revealed that lifetime increases strongly if the damage contribution of the environment is excluded.

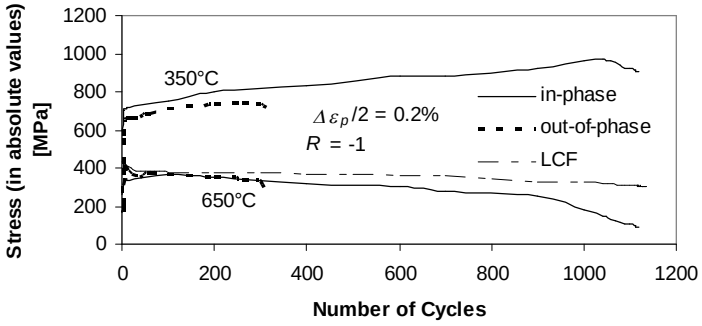

Figure 51 Peak and valley stresses (in absolute values) of TMF tests on Ti6242, values for the isothermal test at 650°C are also included. IP/OP-ratio is about 3.5

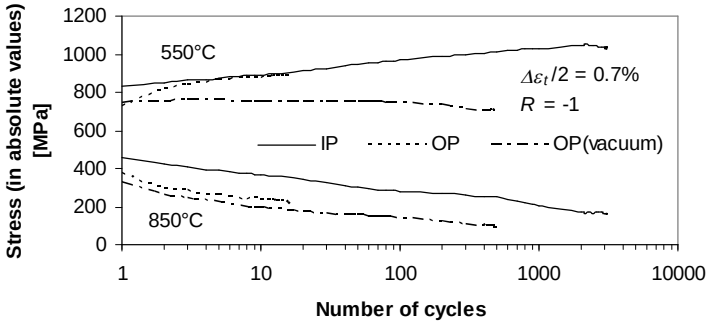

Figure 52 TMF behaviour of TNB-V2, stresses given in absolute values. IP/OP-ratio is about 200, OP_{vac}/OP_{air}-ratio is about 30

9 Non-Destructive Testing and Structural Health Monitoring

9.1 Theory of Measuring Stress Concentration

L. G. Gelimson (RUAG)

Directly measuring stresses at zones of their concentration [1] by means of real physical devices with nonzero sizes such as strain gages leads to dangerously underestimating maximum stresses because of averaging the experimental data within measuring elements of the devices.

The purpose of the present theory is to reliably define true maximum stresses at their concentration zones. This purpose is achieved by designing and applying adequately modeling stress and strain states in typical elasticity problems on stress concentration. The distinctive feature of the proposed theory to measure stress concentrations is using the following new calculation formulas to determine true maximum stresses at concentration. The obtained experimental stress should be multiplied by the corresponding factor determined by solving the corresponding elasticity problem.

The Kirsch problem [2, 3] is determining stress concentration on the boundary of a round hole in a theoretically infinite plate extended in one direction x at infinity. The maximum stress holds on two generatrixes of the hole with radius r. But a strain gage best placed on the surface of the hole has a measuring mesh of a nonzero length $2rl$ (via introducing the corresponding number l) on which averaging takes place. To determine the true maximum stress, the measured stress has to be multiplied by the factor [4, 5]

$$K = 3/(1 + l^{-1}\sin 2l).$$

Let two stresses σ_x, σ_y extend the plate in orthogonal directions x and y, and a uniform pressure p hold in the hole. By considering the Poisson ratio μ of the plate material and the transverse sensitivity μ_t of the measuring mesh of the device at the same place, the factor is [4]

$$K = [(1 + 2\mu)p + 3\sigma_y - \sigma_x)]/ \{(1 + 2\mu - \mu_t)p + (1 - \mu\mu_t) [\sigma_x + \sigma_y - l^{-1}\sin 2l\ (\sigma_x - \sigma_y)]\}.$$

If the measuring mesh with width βr is placed on a side of a plate with distance δr (δ a number) from the hole by x as a mesh symmetry axis, the factor is [4]

$$K = [(1 + 2\mu)p + 3\sigma_y - \sigma_x)]/\{\mu(1 + \mu_t)p +$$
$$(\mu_t - \mu)\sigma_x + (1 - \mu\mu_t)\sigma_y + [(1 + \mu)(1 - \mu_t)p +$$
$$0.5(-1 + 3\mu - 3\mu_t + \mu\mu_t)\sigma_x + 0.5(3 - \mu +$$
$$3\mu_t - 3\mu\mu_t)\sigma_y]/(\beta l)[\arctan l(1 + \delta)^{-1} -$$
$$\arctan l(1 + \delta + \beta)^{-1})] + (1 + \mu)(1 - \mu_t)(\sigma_x - \sigma_y)/\beta$$
$$[(1 + \delta)((1 + \delta)^2 + l^2)^{-1} - (1 + \delta + \beta)((1 + \delta + \beta)^2 + l^2)^{-1} -$$
$$1.5(1 + \delta)((1 + \delta)^2 + l^2)^{-2} + 0.75(1 + (1 + \delta + \beta)^2(1 + \delta)^{-2})$$
$$(1 + \delta + \beta)((1 + \delta + \beta)^2 + l^2)^{-2} + (1 + \delta)((1 + \delta)^2 + l^2)^{-2} -$$

$(1 + \delta)^2 + l^2)(1 + \delta)^{-2}(1 + \delta + \beta)^3((1 + \delta + \beta)^2 + l^2)^{-3}$ -

$0.5\beta(1 + \delta + 0.5\beta)(1 + \delta + \beta)(3(1 + \delta + \beta)^2 - l^2)(1 + \delta)^{-2}$

$((1 + \delta + \beta)^2 + l^2)^{-3}]\}$.

For a round plate of radius *r* supported on the boundary and loaded by a one-side uniform pressure, for the true greatest stress at the center of the opposite side of the plate, the factor is [4]

$K = 1/(1 - l^2)$.

If the same plate is fixed on the boundary, the factor is [4]

$K = 1/[1 - (1 + \mu)/(3 + \mu)l^2]$.

For an infinitely long cylindrical shell with radius *a* and thickness *h* fixed on one edge, by measuring the greatest axial stress on the internal surface at the edge, the factor is [4]

$K = kl \exp kl / \sin kl$

where

$k = [3(1 - \mu^2)]^{1/4}/(ah)^{½}$.

For other types of stress concentration, the corresponding elasticity problems should be preliminarily solved. The proposed means of measuring maximum stresses at stress concentration zones apply to many problems in measurement technology and are especially useful and even urgent in modern engineering with extreme loading conditions.

[1] Handbuch Struktur-Berechnung. Prof. Dr.-Ing. L. Schwarmann. Industrie-Ausschuss-Struktur-Berechnungsunterlagen, Bremen, 1998

[2] Kirsch, G.: Die Theorie der Elastizität und die Bedürfnisse der Festigkeitslehre. VDI Z., 42 (1898), 797-807

[3] Peterson's Stress Concentration Factors (2nd Edition). By: Pilkey, Walter D. John Wiley & Sons, 1997

[4] Gelimson, L. G.: Elastic Mathematics. General Strength Theory. The ”Collegium” International Academy of Sciences Publishers, Munich (Germany), 2004

[5] Gelimson, L. G.: Equivalent Stress Concentration Factor. In: Review of Aeronautical Fatigue Investigations in Germany During the Period March 2003 to March 2005, Dr. Claudio Dalle Donne, EADS Corporate Research Center Germany, SC/IRT/LG-MT–2005-039 Technical Report, 30-32